RESEARCH ARTICLE

Key Points:
- We examine Saturn's planetary period oscillations (PPOs) in magnetic and SKR data over 2013-2015
- North and south periods near coalesced from mid-2013 to mid-2014 increasing from ~10.66 to 10.70 h
- North period then increased to ~10.78 h resulting in a reversal in periods that endured to end 2015

Correspondence to:
G. Provan,
gp3@ion.le.ac.uk

Planetary period oscillations in Saturn's magnetosphere: Coalescence and reversal of northern and southern periods in late northern spring

G. Provan[1], S. W. H. Cowley[1], L. Lamy[2], E. J. Bunce[1], G. J. Hunt[1], P. Zarka[2], and M. K. Dougherty[3]

[1]Department of Physics and Astronomy, University of Leicester, Leicester, UK, [2]LESIA, Observatoire de Paris, CNRS, UPMC, Université Paris Diderot, Meudon, France, [3]Blackett Laboratory, Imperial College London, London, UK

Abstract We investigate planetary period oscillations (PPOs) in Saturn's magnetosphere using Cassini magnetic field and Saturn kilometric radiation (SKR) data over the interval from late 2012 to the end of 2015, beginning ~3 years after vernal equinox and ending ~1.5 years before northern solstice. Previous studies have shown that the northern and southern PPO periods converged across equinox from southern summer values ~10.8 h for the southern system and ~10.6 h for the northern system and near coalesced ~1 year after equinox, before separating again with the southern period ~10.69 h remaining longer than the northern ~10.64 h. We show that these conditions ended in mid-2013 when the two periods coalesced at ~10.66 h and remained so until mid-2014, increasing together to longer periods ~10.70 h. During coalescence the two systems were locked near magnetic antiphase with SKR modulations in phase, a condition in which the effects of the generating rotating twin vortex flows in the two ionospheres reinforce each other via hemisphere-to-hemisphere coupling. The magnetic-SKR relative phasing indicates the dominance of postdawn SKR sources in both hemispheres, as was generally the case during the study interval. In mid-2014 the two periods separated again, the northern increasing to ~10.78 h by the end of 2015, similar to the southern period during southern summer, while the southern period remained fixed near ~10.70 h, well above the northern period during southern summer. Despite this difference, this behavior resulted in the first enduring reversal of the two periods, northern longer than southern, during the Cassini era.

1. Introduction

A unique feature of Saturn's magnetosphere is the ubiquitous modulations observed throughout the system near the ~10.6 h planetary rotation period, despite the close axisymmetry of the internal planetary magnetic field [*Burton et al.*, 2010]. These "planetary period oscillations" (PPOs) were first observed in auroral Saturn kilometric radiation (SKR) emissions by the Voyager spacecraft during approach to the planet [*Warwick et al.*, 1981, 1982; *Desch and Kaiser*, 1981], and subsequently in magnetospheric energetic particle and magnetic field data, as well as in ultraviolet auroral emissions [*Carbary and Krimigis*, 1982; *Sandel and Broadfoot*, 1981; *Sandel et al.*, 1982; *Espinosa and Dougherty*, 2000]. It was later discovered in SKR emissions observed remotely from the planet by the Ulysses spacecraft that the period of the modulations varies by up to ~1% over few year intervals [*Galopeau and Lecacheux*, 2000], much too fast a rate to be associated directly with the rotation of the planet. A principal finding of the Cassini mission has been that two distinct periods are generally present, one associated with the Northern Hemisphere and the other with the southern [*Kurth et al.*, 2008; *Gurnett et al.*, 2009a; *Andrews et al.*, 2010b; *Southwood*, 2011; *Cowley et al.*, 2016]. Cassini observations have also shown that the modulations in the magnetic field, SKR, and auroral hiss emissions are fundamentally rotational in nature, rotating around the planet's axis in the sense of planetary rotation at the northern and southern PPO periods [*Cowley et al.*, 2006; *Southwood and Kivelson*, 2007; *Andrews et al.*, 2008, 2010a, 2011; *Gurnett et al.*, 2009b; *Lamy*, 2011; *Lamy et al.*, 2013].

A principal characteristic property of the PPOs is evidently their rotation period, which has been monitored near continuously during the Cassini mission using observations of both magnetic field oscillations and SKR modulations, whose significant variations are updated in this paper to the end of 2015. In Figure 1 we show the form of the two magnetic PPO systems, where the blue arrowed lines and symbols show the perturbation magnetic fields, the green arrowed lines and symbols the associated current systems, and the black arrowed lines the background magnetic field, to a first approximation axisymmetric about the vertical
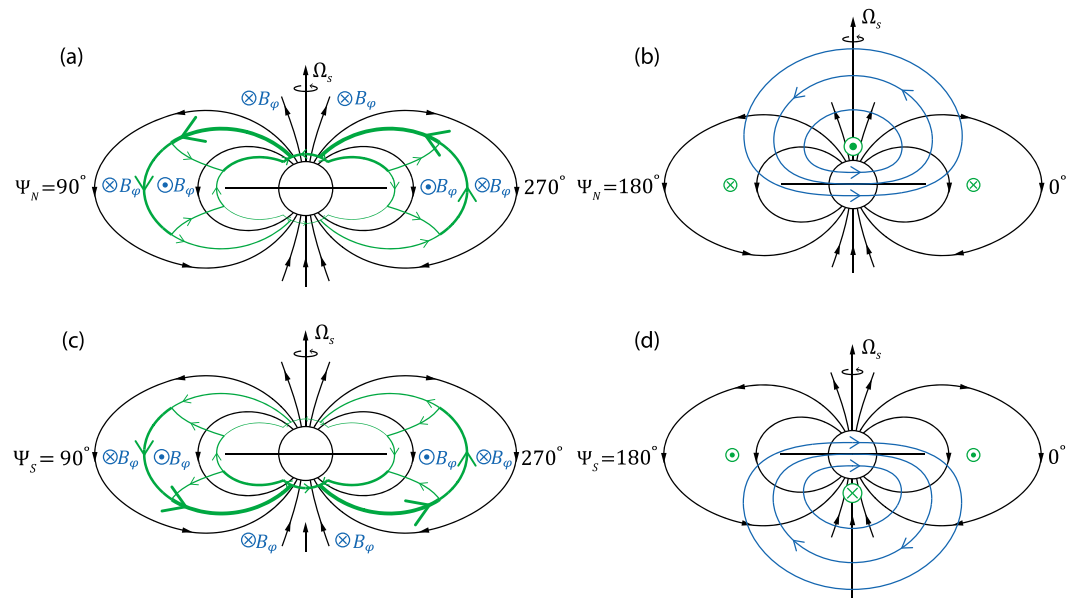
Figure 1. Sketches showing the electric currents and perturbation magnetic fields of the PPO phenomenon in Saturn's magnetosphere. Green arrowed lines and symbols indicate electric currents, blue arrowed lines and symbols indicate the associated perturbation magnetic fields, while black arrowed lines show the background magnetospheric magnetic field. Circled dots and crosses show vectors pointing out of and into the plane of the figure, respectively. (a and b) The northern PPO system, and (c and d) the southern PPO system. Figures 1a and 1c show the $\Psi_{N,S} = 90° - 270°$ meridian planes as indicated, while Figures 1b and 1d show the $\Psi_{N,S} = 0° - 180°$ meridian planes, corresponding to Figures 1a and 1c viewed from the left. (Adapted from *Cowley and Provan* [2015].)

spin/magnetic axis of the planet [*Southwood and Kivelson*, 2007; *Andrews et al.*, 2008, 2010a, 2010b, 2012; *Provan et al.*, 2009, 2011; *Southwood and Cowley*, 2014; *Hunt et al.*, 2014, 2015]. Figures 1a and 1b correspond to the northern system and Figures 1c and 1d to the southern system, shown in two orthogonal meridians that best display the current systems and the perturbation fields, respectively. Figures 1b and 1d correspond to Figures 1a and 1c, respectively, as viewed from the left. The primary currents flow along field lines into the ionosphere on one side of the planet and out on the other, closing both within the body of the magnetosphere and in the two ionospheres (Figures 1a and 1c). These currents produce perturbation fields that are quasi-uniform within the equatorial region, and close in quasi-dipolar fields transverse to the spin/magnetic axis over each corresponding pole. With increasing time each system rotates about the planetary axis with its corresponding PPO rotation period, near that of the planetary rotation period. The perturbation fields in the equatorial region thus consist of the vector sum of the perturbations due to the two systems, which show interference effects at the beat period of the two oscillations that become pronounced when the amplitudes of two systems are near equal [*Provan et al.*, 2011, 2013; *Andrews et al.*, 2012; *Cowley et al.*, 2015]. The perturbations in each polar region, however, display only the single periods of their corresponding system, to within a ~10% limit by amplitude [*Andrews et al.*, 2012; *Hunt et al.*, 2015]. The two PPO periods can then be derived from orbit-to-orbit determinations of the oscillation phase of the three field components on few day periapsis passes through the "core" region of the magnetosphere (dipole $L \leq 12$) on near-equatorial orbits, or on open field lines over the two polar regions on highly inclined orbits, as will be described further in section 2.

With regard to the radio observations, SKR is mainly generated in the extraordinary mode by the cyclotron maser instability of auroral electrons accelerated in regions of upward directed field-aligned current [*Lamy et al.*, 2010, 2011; *Mutel et al.*, 2010]. PPO-related modulations of the emission in the Northern and Southern Hemispheres are thus thought to be due to related modulations of the auroral field-aligned currents by the rotating PPO current systems illustrated in Figure 1 [*Hunt et al.*, 2014, 2015]. SKR is beamed along a thin hollow cone at large angles from the magnetic field direction from its sources on auroral field lines, with the northern sources illuminating the region to ~20° south and the southern sources the region to ~20° north, such that both can be observed within ~20° latitude either side of the equator, outside of a shadow zone extending to ~4 R_S in the equatorial plane [*Lamy et al.*, 2008a, 2008b, 2009; *Cecconi et al.*,

2009; *Kimura et al.*, 2013]. (R_S is Saturn's 1 bar equatorial radius, equal to 60,268 km.) Northern and southern emissions can be distinguished in this region by their state of circular polarization, right hand (RH) from the Northern Hemisphere and left hand (LH) from the southern as measured both remotely [*Kaiser et al.*, 1984; *Lamy et al.*, 2008a; *Fischer et al.*, 2009] and in situ [*Lamy et al.*, 2010, 2011; *Menietti et al.*, 2011]. For near-equatorial observations outside the shadow zone, observable sources are also restricted by the conical beaming to two narrow bands of local time (LT) located ~4 h LT either side of the observing point [*Lamy et al.*, 2008b, 2009; *Cecconi et al.*, 2009]. SKR source strength also varies significantly with LT, being strongest in the midmorning sector peaking at ~8 h LT and weakest at approximately opposite LTs in the postdusk sector [*Lamy et al.*, 2009]. This, combined with the restricted viewing in LT at any particular observation point, leads to strobe-like SKR modulations being observed throughout the near-equatorial dawn sector from postmidnight to noon, despite the fundamentally rotational nature of the SKR modulations [*Andrews et al.*, 2011; *Lamy*, 2011; *Lamy et al.*, 2013]. PPO periods are determined by spectral analysis of the modulated SKR power, which by virtue of their directly related physical origin are in principle expected to be essentially identical to those determined from analysis of magnetic field data.

Closely similar periods, typically to within ~20 s, have indeed been derived from magnetic field and SKR data during the initial phase of the Cassini mission in 2004–2008 under postsolstice southern summer conditions, when the two periods were found to be separated by ~12–14 min, ~10.6 h for the northern system, and ~10.8 h for the southern [*Gurnett et al.*, 2009a, 2011; *Andrews et al.*, 2010b, 2011, 2012; *Lamy*, 2011]. However, in late 2008 the two periods began to move slowly toward a common value, reaching ~10.65 h for the northern system and ~10.75 h for the southern system by the time of vernal equinox in August 2009. The postequinox behavior has been more difficult to discern and consequently the subject of some discussion. *Gurnett et al.* [2010, 2011] suggested on the basis of SKR measurements that the slow convergence in periods continued across vernal equinox, leading to near coalescence of the periods in early 2010, 7 months after equinox, and to subsequent reversal. The latter suggestion was supported by analysis of earlier Ulysses SKR data which appeared to show a similar convergence and a clear reversal over the interval between 1994 and 2000 spanning the previous spring equinox in late 1995. The interpretation of the Ulysses data is subject to some uncertainty, however, because the hemisphere of SKR emission was not determined by polarization measurements. Analysis of polarization-separated Cassini SKR data by *Lamy* [2011] also indicates a near coalescence in northern and southern SKR periods in early to mid-2010. Cassini magnetic field measurements, however, indicate that the two slowly converging periods approached a near-common value of ~10.68 h approximately 1 year after equinox but then separated again by ~3 min with the northern period ~10.64 h remaining shorter than the southern ~10.69 h [*Andrews et al.*, 2012; *Provan et al.*, 2013]. Similar conditions of small ~2–4 min period separations, southern longer than northern, were then maintained over the following ~3 year interval until mid-2013 but were characterized by abrupt transitions in the relative amplitude of the northern and southern oscillations at intervals of ~100–200 days, combined with small changes in the periods [*Provan et al.*, 2013, 2014]. While the northern oscillations were found to be weaker than the southern by a factor of ~2.5 in the pre-equinox southern summer data [*Provan et al.*, 2011; *Andrews et al.*, 2012] and grew in amplitude to become near equal to the southern during the transequinox interval of slowly converging periods [*Andrews et al.*, 2012; *Provan et al.*, 2013], the subsequent transitions during the postequinox interval of smaller period separations saw the abrupt reemergence of southern dominance by a factor of ~3, followed by northern dominance with no evidence of southern oscillations being present, and then intervals of weaker northern and southern dominance [*Provan et al.*, 2013, 2014]. Corresponding analyses of SKR data over this interval have also shown a good measure of agreement [*Provan et al.*, 2014; *Fischer et al.*, 2014; *Cowley and Provan*, 2015]. Overall, these SKR and magnetic field results indicate that while the two PPO periods came close to coalescence in the immediate postequinox interval in 2010 and may even have undergone short intervals of weak period reversal as suggested by both polarization-separated SKR data [*Lamy*, 2011] and magnetic field data [*Cowley and Provan*, 2015], a clear reversal to well-separated periods similar to that suggested by the Ulysses data following the previous spring equinox did not take place during the interval to at least ~4 years following vernal equinox in mid-2009.

We note, however, that *Fischer et al.* [2015] have presented a somewhat contrary view based on polarization-separated SKR data in which the northern and southern periods reversed sense directly after vernal equinox for an interval of ~8 months, approximately north for south and vice versa, subsequently displaying intermittent intervals of coalesced periods. *Cowley and Provan* [2016] have argued that these discrepancies arise

largely from misinterpretation of the polarization-separated SKR data that can sometimes remain dual modulated at both northern and southern periods, as shown in the prior study by *Lamy* [2011]. The precise origin of this dual modulation remains at present unclear, however, though we note that dual modulation of the field-aligned currents has previously been demonstrated in high-latitude magnetic field data by *Hunt et al.* [2015].

In this paper we examine magnetic field and SKR data spanning the ~3 year interval from late 2012 to the end of 2015, thus beginning ~3 years after vernal equinox and ending ~1.5 years before northern solstice in mid-2017, which interfaces and modestly overlaps with the related study by *Provan et al.* [2014]. We show that following the ~3 year postequinox interval between mid-2010 and mid-2013 in which the periods were closely spaced but with the southern period remaining longer than the northern, as outlined above, the two periods near coalesced at an intermediate value over a ~1 year interval until mid-2014 and then enduringly reversed, northern longer than southern, for the first time during the Cassini era.

2. PPO Properties From Magnetic Field Data

2.1. Magnetic Data Analysis Procedures

The methodology employed to derive the phases of the northern and southern PPO oscillations from Cassini magnetic field data has been discussed at length by *Andrews et al.* [2012] and *Provan et al.* [2013, 2014], such that only a brief outline will be presented here. Position with respect to the northern and southern PPO systems is defined by the azimuthal parameters Ψ_N and Ψ_S, respectively, shown in Figure 1, where both are defined to be zero (modulo 360°) on the meridians where their respective equatorial quasi-uniform fields point radially outward from the planet (the right-hand side of Figures 1b and 1d), and to increase clockwise around the planet as viewed from the north, such that their values increase with time at a fixed point as the systems rotate. Consideration of the perturbation fields expressed in spherical polar components referenced to the planet's northern spin/magnetic axis, as employed throughout this paper, shows that in the equatorial region the radial (r) components of the two systems vary as $\sim \cos \Psi_{N,S}$, while those of the two azimuthal (φ) fields vary as $\sim \sin \Psi_{N,S}$ in lagging quadrature with r, the signature of a quasi-uniform field. The colatitudinal (θ) field components, however, vary as $\sim - \cos \Psi_N$ for the northern system, in antiphase with r, and as $\sim \cos \Psi_S$ for the southern system, in phase with r. Thus, at points in the beat cycle when the two systems are in phase, $\Psi_N = \Psi_S$ modulo 360°, the r and φ components of the two systems add while the θ components subtract, and vice versa when the two systems are in antiphase, $\Psi_N = \Psi_S \pm 180°$ modulo 360°. In the two polar regions the phases of the r and θ components remain the same as for the corresponding equatorial perturbations, while the φ component reverses sign across the main PPO-related field-aligned current sheets to vary as $\sim - \sin \Psi_{N,S}$ in leading quadrature with r, the signature of a transverse quasi-dipolar field. As shown in Figures 1a and 1c, the directions of the main field-aligned currents are directed from north to south along the field at $\Psi_{N,S} = 90°$, upward with respect to the northern ionosphere and downward with respect to the southern, and from south to north along the field at $\Psi_{N,S} = 270°$, downward with respect to the northern ionosphere and upward with respect to the southern, as demonstrated directly by *Hunt et al.* [2014, 2015] from analysis of high-latitude field data.

The orientation of each system with respect to the Sun at any time t is then given by the empirically determined phase functions $\Phi_{N,S}(t)$, which define the azimuth relative to noon in which the quasi-uniform equatorial field of each system points radially outward at that time, i.e., the azimuth relative to noon of the $\Psi_{N,S} = 0°$ (modulo 360°) meridians. The relationship between the two azimuthal functions is then given by

$$\Psi_{N,S}(\varphi, t) = \Phi_{N,S}(t) - \varphi, \tag{1}$$

where φ is azimuth with respect to noon, increasing around the planet in the sense of planetary rotation. The rotation period of the system is then

$$\tau_{N,S} = \frac{360}{\left(\frac{d\Phi_{N,S}}{dt}\right)}, \tag{2}$$

where the phases $\Phi_{N,S}(t)$ are expressed in degrees.

To determine phases $\Phi_{N,S}(t)$ from the magnetic field data, we select few day intervals of data on each spacecraft revolution (Rev) that correspond either to the quasi-dipolar core region of the magnetosphere

(dipole $L \leq 12$) on the periapsis passes of near-equatorial orbits, or to the northern and southern "polar void" regions observed on highly inclined orbits [e.g., *Andrews et al.*, 2010b; *Jinks et al.*, 2014]. These data are band pass filtered between periods of 5 and 20 h to extract the PPO-related signals, corresponding to the combined quasi-uniform fields of the northern and southern systems for near-equatorial data and to the separate quasi-dipolar perturbations of the northern and southern systems for polar data. In some instances on highly inclined orbits when periapsis passage through the equatorial region is at sufficiently small radial distance, $\sim 10\,R_S$ or less, it is also possible to observe the near-equatorial perturbation field typically over some fraction of a PPO cycle [*Andrews et al.*, 2010b, 2012; *Provan et al.*, 2014]. While the near-equatorial variations observed in the r and θ components on such passes are dominated by spatial effects associated with the ring current, PPO-related perturbations can be retrieved from unfiltered azimuthal field data to which neither the planetary field nor the near-axisymmetric inner ring current contribute. Both filtered polar and filtered and unfiltered equatorial data are employed in this study, some representative examples of which are shown in Appendix A, obtained during various of the mission intervals to be outlined in section 2.2.

The selected data, processed as above, are least squares fitted to the rotating function:

$$B_i(\varphi,\ r,\ t) = B_{0i} \cos(\Phi_g(r,\ t) - \varphi - \psi_i), \tag{3}$$

where φ is again azimuth measured from noon, and Φ_g is a "guide phase" function taken for simplicity to correspond to a fixed rotation period τ_g close to that of the oscillations. Specifically, within the core magnetosphere we take

$$\Phi_g = \frac{360\ t}{\tau_g} \quad \text{deg}, \tag{4a}$$

where t is time since 00 UT on 1 January 2004, while for radial distances r beyond $12\,R_S$ on open field lines we also include a term that takes account of the finite radial downtail propagation speed:

$$\Phi_g = \frac{360\ t}{\tau_g} - G(r - 12\ R_S) \quad \text{deg}, \tag{4b}$$

where phase gradient $G = 3$ deg R_S^{-1} is based on the results of *Arridge et al.* [2011] and *Provan et al.* [2012]. The outputs of the fitting procedure are the amplitude of the oscillations B_{0i} and the relative phase ψ_i for (in general) each of the three field components i, corresponding to r, θ, and φ (see examples in Appendix A). Uncertainties in the relative phases are estimated to be typically $\pm 10°$ [e.g., *Andrews et al.*, 2012]. The Rev-to-Rev relative phase measurements ψ_i are then used to construct an overall model of the northern and southern PPO phases $\Phi_{N,S}(t)$, as discussed in section 2.3, from which the periods follow from equation (2).

2.2. Cassini Orbital Parameters

The nature of the magnetic phase data obtained, whether dual-modulated equatorial or single-modulated polar, clearly depends on the spacecraft orbit. In Figure 2 we overview the main orbital parameters over the ~ 3 year study interval, together with some seasonal data. The interval comprises $t = 3199 - 4383$ days as shown at the bottom of the figure, where $t = 0$ again corresponds to 00 UT on 1 January 2004, thus spanning from 4 October 2012 to 31 December 2015 inclusive. It includes data from Cassini Revs 173 to 229, as indicated at the top of the plot, where Rev numbers, defined from apoapsis to apoapsis, are indicated at the times of periapsis. Year boundaries are also indicated in red. The interval interfaces and modestly overlaps with that of the prior related study by *Provan et al.* [2014], who analyzed data from the interval $t = 1827 - 3510$ days corresponding to 1 January 2009 to 10 August 2013 inclusive, employing data from Cassini Revs 99 to 195.

Figure 2a first shows the latitude of the Sun at Saturn, varying between $\sim 13°$ and $\sim 21°$ over the interval, which began ~ 3.2 years after vernal equinox in mid-August 2009 and ended ~ 1.4 years before northern solstice in late May 2017, when the solar latitude will reach its maximum value of $\sim 27°$. The polar auroral regions, extending to $\sim 16°$ colatitude in the Northern Hemisphere and $\sim 18°$ in the southern, are thus predominantly in sunlight in the Northern Hemisphere and in darkness in the Southern Hemisphere during the interval, essentially the reverse of the postsouthern solstice situation at the start of the Cassini orbital mission in 2004/2005.

Figure 2b shows the latitude range on each Rev, plotted at the time of periapsis, together with the latitudes of periapsis (blue circles) and apoapsis (red circles). The orbit was highly inclined at the start of the interval, with
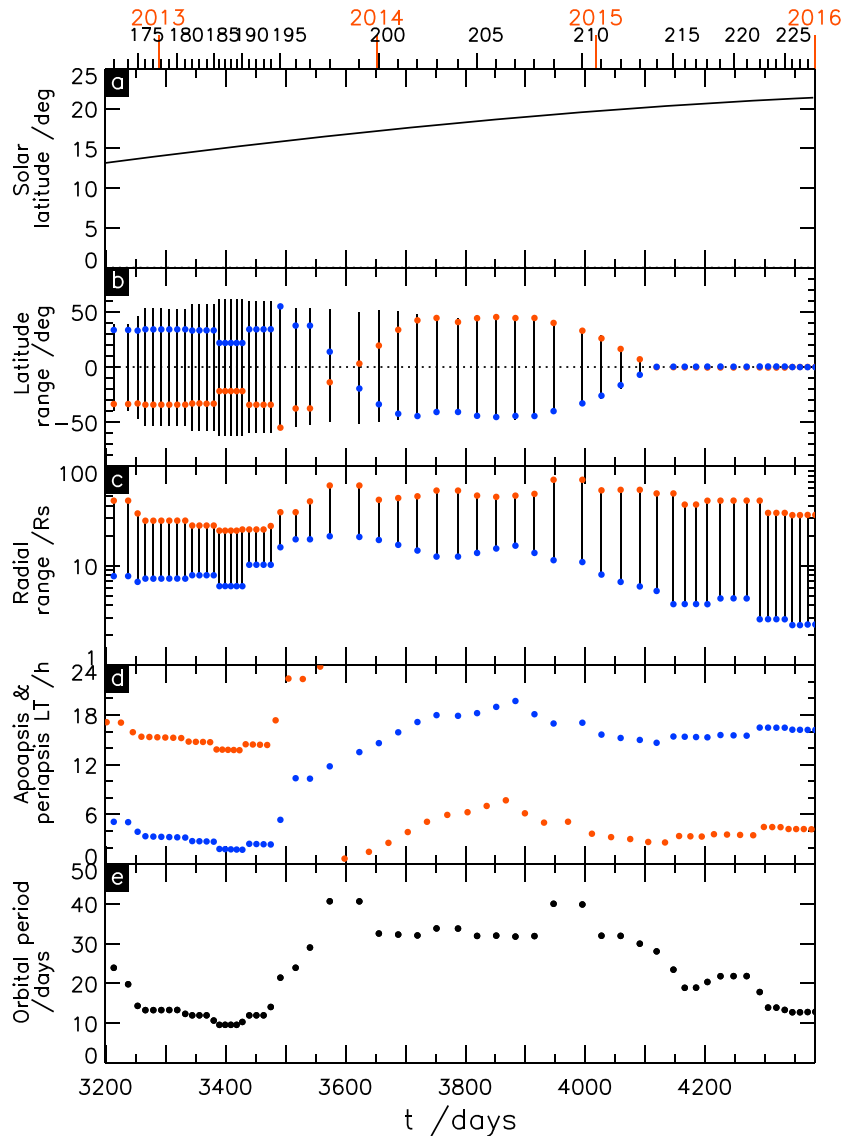
Figure 2. Plot showing seasonal and Cassini orbital parameters over the ~3 year interval of the study spanning $t = 3199 - 4383$ days, where $t = 0$ corresponds to 00 UT on 1 January 2004 (4 October 2012 to 31 December 2015 inclusive). Year markers are shown in red at the top of the plot, together with Cassini Rev numbers defined from apoapsis to apoapsis, plotted at periapsis, and numbered every five Revs. (a) The planetocentric latitude of the Sun at Saturn (degree), corresponding to northern spring conditions. (b) The vertical bars in Figure 2 show the latitude range on each Rev (degree), plotted at the time of periapsis, with the blue circle corresponding to the latitude of periapsis, and the red circle to the latitude of apoapsis. (c) The radial range on each Rev on a log scale (R_S), also plotted at the time of periapsis. (d) The LT (hour) of apoapsis (red circles) plotted at the time of apoapsis, and the LT of periapsis (blue circles) plotted at the time of periapsis. (e) The orbital period of each Rev (days) plotted at the time of periapsis.

apoapsis initially in the Southern Hemisphere, then moving into the Northern Hemisphere near the end of 2013. Near the beginning of 2015, however, the orbit became closely equatorial and remained so to the end of the interval. The magnetic data thus mainly correspond to individual north and south phase measurements from filtered north and south polar data from near the start of the interval to near the start of 2015 and to the phases of dual-modulated equatorial oscillations from filtered equatorial data during the remainder of the interval (starting at Rev 211). Figure 2c shows the radial range on each Rev on a log scale, also plotted at the time of periapsis. It can be seen that periapsis was at a radial distance of ~10 R_S or less on the initial set of inclined orbits from the start of the interval to mid-2013, thus also allowing phase determinations from relatively brief near-equatorial segments of unfiltered azimuthal field data (to Rev 194). Periapsis then moved to

larger radial distances for the remainder of the inclined orbits, allowing only polar phases to be determined, before returning to smaller values ~5 R_S as the orbit returned to the equatorial plane. In Appendix A we exemplify the magnetic field data and fits to equation (3) for each of these three regimes of spacecraft orbit.

Figure 2d shows the LT of both periapsis (blue circles) and apoapsis (red circles), relevant to the LT of the conically beamed SKR sources visible to the spacecraft, as discussed in section 1. Apoapsis was initially located in the dusk to postnoon sector but then moved near the end of 2013 into the midnight to dawn sector for the remainder of the interval. SKR emissions observed on the near-equatorial orbits later in the interval are thus expected to be dominated by the mid-morning sources near ~8 h LT that give rise to strobe-like PPO modulations throughout the postmidnight to noon sector. If the observed SKR maxima on these Revs correspond to times when the upward field-aligned currents in Figure 1 are centered on these dominant sources, as expected, then northern SKR maxima should occur when the quasi-uniform field of the northern system points radially outward postnoon, i.e., when the northern magnetic phase has values around $\Phi_N \approx 30°$ (modulo 360°) corresponding to ~14 h LT, while southern SKR maxima should occur when the quasi-uniform field of the southern system points radially outward postmidnight, i.e., when the southern magnetic phase has values around $\Phi_S \approx 210°$ (modulo 360°), corresponding to ~2 h LT.

Figure 2e also shows the spacecraft orbital period, relevant to the cadence of the Rev-to-Rev magnetic phase measurements, and hence to the issue of aliasing of the PPO periods derived from them, discussed in section 2.3 and Appendix B. Periods are as short as ~10 days early in the interval, lengthen to ~30–40 days midinterval, and fall again to ~15 days toward the end of the interval.

2.3. Derivation of Magnetic Field Phases and Periods

Figures 3a and 3c show the northern and southern fitted phases ψ_i (equation (3)), respectively, relative to a guide phase with a fixed period of 10.70 h (equations (4a) and (4b)). Two cycles of phase are shown on the vertical axis in each plot to aid visualization of data continuity, with each data point being plotted twice. Red, green, and blue circles correspond to the phases of the r, θ, and φ field components, respectively, with the open circles corresponding to polar data and the solid circles to equatorial data. The polar data correspond to the individual hemispheres concerned, northern in Figure 3a and southern in Figure 3c, while the same equatorial measurements are shown in both plots, transformed into "N-format" in Figure 3a and "S-format" in Figure 3c, as outlined below. Phases are not displayed in cases where the fit to equation (3) is poor, such that the RMS deviation of the data from the best fit model is significantly larger than the amplitude, and where the measured amplitude is very small such that the phase becomes unreliable, typically an issue for polar data with measured amplitudes less than ~0.05 nT (see, e.g., Appendix A).

In Figures 3a and 3c the phases of the r component oscillations are shown as measured in all cases, while the phases of the θ and φ components have been transformed into either N-format (Figure 3a) or S-format (Figure 3c). In N-format the phases of the θ and φ components are transformed such that they would have the same value as the r component for a pure northern oscillation according to the discussion of Figure 1 in section 2.1, while in S-format they are similarly transformed such that they would have the same phase as the r component for a pure southern oscillation. That is to say, in N-format the θ component phase is shifted by 180° since it is in antiphase with r for the northern system (Figure 1b), while in S-format the θ phase is shown as measured since it is in phase with r for the southern system (Figure 1d). On the same basis the phase of the φ component is shifted by +90° for all polar data, since in the polar region it is in leading quadrature with r in both polar regions, and by −90° for all equatorial data, since in the equatorial region it is in lagging quadrature with r for both systems (Figures 1a and 1c). Given the validity of these phase relationships, for polar data these transformations should bring the phases of all three field components for each Rev into equality within measurement errors, corresponding to the phase of the r component. For the combined oscillations present in the equatorial data, the transformed phases cluster about the northern r component phase in N-format and about the southern r component phase in S-format, as shown by *Andrews et al.* [2012] and *Provan et al.* [2013]. This allows both phases to be determined provided that one oscillation is not too weak relative to the other. Given typical ~10° uncertainties in the individual phase determinations, a typical limit is that the amplitude of one oscillation should not be less than ~20% of that of the other [*Provan et al.*, 2013]. If this condition is not met, the phase modulation due to the weaker signal cannot be discerned within the uncertainties in the data, and only the phase of the stronger oscillation can then be determined.
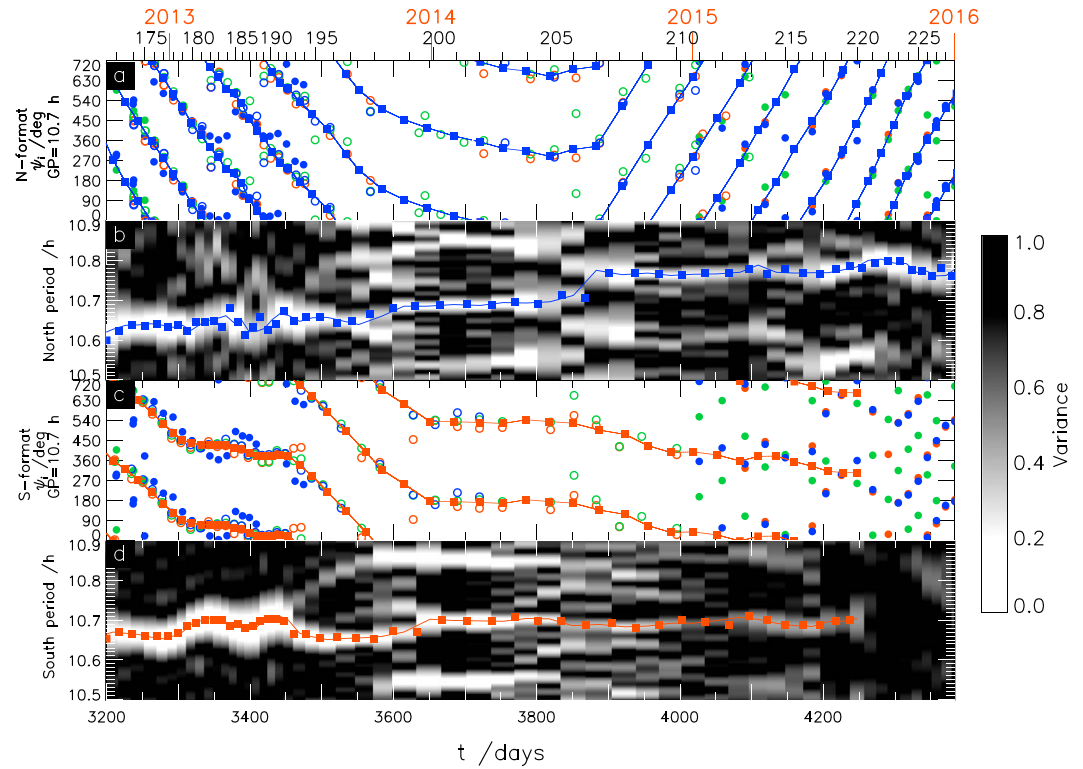
Figure 3. Plot showing measured and modeled magnetic PPO phases and periods over the same ~3 year study interval as in Figure 2. Year markers and Rev numbers are shown at the top of the plot in the same format as Figure 2. (a) Magnetic field phases (degree) in N-format (see text) relative to a guide phase of 10.70 h period (equations (4a) and (4b)), where open circles correspond to northern polar data and filled circles to equatorial core region data. Two cycles of phase are shown on the vertical axis with each data point being plotted twice. Red, green, and blue open and filled circles correspond to the r, θ, and φ spherical polar field components, respectively, referenced to the northern spin and magnetic axis. Blue squares joined by straight lines show the northern PPO phase model relative to the guide phase, obtained from 5 Rev (or occasionally 3 Rev) linear fits to these data using directional statistics methods (section 2.3). (b) The fit variances (equation (7)) for modulation periods between 10.5 and 10.9 h, gray scaled as shown on the right. The blue solid line traces a near-continuous variance minimum, generally a global minimum within the range, but sometimes a local minimum as discussed in the text, taken to be the northern PPO period. The center phase of each fit corresponds to the blue squares shown in Figure 3a. The blue squares in Figure 3b show the periods determined from the straight line segments joining the model phase values (squares) in Figure 3a, shown at the center of each segment. (c) Similar to Figure 3a and shows magnetic field phases (degree) in S-format (see text) relative to the same guide phase corresponding to a 10.70 h period, where open circles correspond to southern polar data and filled circles to equatorial core region data. The southern PPO phase model (degree) relative to the guide phase derived from 5 Rev (or occasionally 3 Rev) fits is shown by the red squares joined by red lines. (d) Similar to Figure 3b and shows the fit variances for modulation periods between 10.5 and 10.9 h, also gray scaled according to the scale on the right. The red solid line marking a near-continuous variance minimum is taken to be the southern period, while the red squares show the periods obtained from the straight-line segments joining the phase values shown by the red squares in Figure 3c.

Continuous fits to the N- and S-format relative phase data, $\psi_{N,S}(t)$, then yield the northern and southern magnetic phases in equation (1) as

$$\Phi_{N,S}(t) = \Phi_g(t) - \psi_{N,S}(t) = \frac{360\ t}{\tau_g} - \psi_{N,S}(t), \qquad (5)$$

where the second expression on the right-hand side corresponds to a guide phase of fixed period τ_g. Differing guide phases could in general be employed for N- and S-format data, as, e.g., in *Andrews et al.* [2012], though here we have used a guide phase of fixed period 10.70 h throughout. To determine the phase functions $\psi_{N,S}(t)$, we have used directional statistics methods [*Mardia and Jupp*, 2000] to make piecewise linear fits to the N- and S-format phases, similar to *Andrews et al.* [2012] for the pre- and near-equinox data. Specifically, we have fitted

$$\psi'(t) = \alpha\ t + \beta \qquad (6)$$

to running sets of phase data taken 5 Revs at a time (thus consisting of ~15 independent phase measurements), at steps of one Rev. Such a choice of data interval, rather than a fixed interval of time, for example, has the advantage that the resolution of the resulting period determinations is keyed to the cadence of the available phase data, which depends on the variable spacecraft orbital period (Figure 2e). Investigation of the use of differing numbers of Revs showed that 5 Rev tranches represents a good compromise between smoothed outputs from longer tranches and noisier outputs from shorter tranches. Occasionally, however, we have also employed 3 Rev fits at times when the phase slope (period) changes rapidly with time, to avoid inappropriate fits over the longer 5 Rev interval.

The fitting proceeds by determining the best fit constant β for each of a sequence of phase slopes α, and determining which slope gives the best fit overall with the minimum value of variance V given by

$$V = \frac{1}{N} \sum_{n=1}^{N} \left(1 - \cos\left(\psi_n - \psi'(t_n)\right)\right), \tag{7}$$

where ψ_n are the N transformed phases at center times t_n that are included in the fit. The value of V is zero for a perfect fit and approaches unity when for every value of $\psi_n - \psi'(t_n)$ in the data set there is another value that differs by 180°. Phase slope α (in degrees per unit time) corresponds to oscillation period

$$\tau = \frac{\tau_g}{\left(1 - \frac{\alpha \tau_g}{360}\right)}, \tag{8}$$

where τ_g is the guide period (equations (4a) and (4b)). We note that during the earlier interval up to mid-2013 when phases from both polar and unfiltered φ component equatorial data are available, only the polar data have been employed in the fits shown here. The equatorial data from this interval are employed in section 2.5 to determine the relative amplitude of the two oscillations.

Here we have explored α values corresponding to periods between 10.5 and 10.9 h, at steps of 0.001 h, with results shown for the N-format data in Figure 3b and for the S-format data in Figure 3d. The gray coded bars in these figures centered near the periapsis of each Rev show the variance V of each fit over this range of periods, coded according to the scale on the right. The north and south periods are then, in general, taken to correspond to the period with minimum variance, forming a near-continuous data sequence. As found previously by *Andrews et al.* [2012], however, multiple minima are often present, which can occasionally form a transitory overall minimum variance at a period far from preceding or following values. Particularly notable, for example, are the subsidiary minima between ~3600 and ~3800 days that lie with approximately equal displacements on either side of the central near-continuous sequence of minima in both Figures 3b and 3d. It is shown in the Appendix B that these are due to aliasing resulting from the inescapable modulo 360° ambiguity in the phase difference between Revs, which produces subsidiary minima displaced on either side of the true period by an amount depending inversely on the orbital period of the spacecraft (Figure 2e). In these cases we have constrained the period (α value in equations (6) and (8)) to correspond to a secondary variance minimum closest to the ongoing values.

The periods so obtained are shown by the blue solid line for the northern period in Figure 3b and by the red solid line for the southern period in Figure 3d. The center phases of each of these fits, timed near the periapsis of the center Rev of each of the 5 Rev (or 3 Rev) fits, are shown by the blue squares for the northern phase in Figure 3a and by the red squares for the southern phase in Figure 3c. These phase points have then been joined by linear segments to define the northern and southern model phases versus time, relative to the 10.70 h guide phase. It can be seen that these models generally provide excellent overall fits to the N- and S-format phase measurements, respectively. No values for the southern phase are shown beyond ~4250 days (late August 2015), however, since a continuous minimum in the southern variance values cannot be discerned after this time, corresponding to the lack of clear banding in the S-format phase values evident in Figure 3c. As discussed above, this indicates that the southern amplitude had fallen to less than ~20% of the northern amplitude in the core region equatorial data after this time.

While the solid lines in Figures 3b and 3d thus show the periods derived from individual 5 Rev (or 3 Rev) data fits as just outlined, these values are not generally exactly the same as the periods that may be derived direct from the phase model and equation (2), given by the slopes of the lines joining the phase model data points (squares) in Figures 3a and 3c. To investigate the level of the differences, we have computed the periods

corresponding to these piecewise linear phase slopes and have plotted these values as blue squares in Figure 3b for the northern period and as red squares in Figure 3d for the southern period. In general, these periods lie very close to the blue and red solid lines in these two figures, such that either approach to the period, from direct fits to the phase data or from differentiation of the phase model, gives very similar results, typically to within ~0.003–0.007 h (~10–25 s), comparable to the fit uncertainties discussed below. However, scattered larger discrepancies of ~0.01–0.025 h (~40–90 s) occur for the northern period in the first half of 2013. This is likely due to the relatively short intervals of northern polar data available on these Revs resulting from the southern tilt of apoapsis (Figure 2b), which leads to enhanced uncertainties in the northern phase data at that time.

The uncertainties in the phases and periods in Figure 3 can be estimated from the variance V of the fits. Assuming that the phase deviations from the best linear fits are modest, as is generally the case, the cosine in equation (7) can be expanded to give

$$V \approx \frac{1}{2N} \sum_{n=1}^{N} \left(\psi_n - \psi'(t_n) \right)^2, \tag{9}$$

so that the RMS deviation of the phase values from the fitted line is given (in radians) by

$$\delta\psi_{\mathrm{rms}} \approx \sqrt{2V}. \tag{10}$$

For the northern data the minimum variance values in Figures 3b lie typically in the range ~0.05–0.2, such that the RMS deviation of the phase values, representing a measure of the phase uncertainties, is typically ~20°–35°. Similar values also pertain to the southern data in Figure 3d during the initial interval where the phases are determined from single-period polar data. Due to the weakness of the southern oscillations relative to the northern in the dual-modulated equatorial data after ~4000 days (see section 2.5), however, the minimum variance of the S-format fits increases typically to ~0.5, indicating larger phase uncertainties of ~60°. Beyond ~4250 days the minimum variances increase further toward unity, such that the southern phase then becomes indeterminate as indicated above.

Under the same condition as employed in equation (9), the uncertainty in the period can also be estimated as

$$\delta\tau \approx \frac{\tau^2}{\pi T} \sqrt{\frac{6V}{N}}, \tag{11}$$

where τ is the period, T the length of the data interval corresponding to the fit, V the variance of the fit, and N the number of data points [*Cowley and Provan*, 2016]. This yields typical uncertainties in both periods of ~0.003–0.005 h (~10–20 s) over most of the interval, though rising for the southern period to ~0.0075 h (~30 s) after ~4000 days, before it becomes indeterminate after ~4250 days.

2.4. Comparison of Northern and Southern Magnetic Field Phases and Periods

To compare these results more closely, in Figure 4 we show northern (blue) and southern (red) phase and period data plotted together. Figure 4a shows the phases relative to the common guide phase of 10.70 h period from Figures 3a and 3c, while Figure 4b shows the periods from Figures 3b and 3d. Figure 4c then shows the difference between the two phases, that is to say the "beat phase" defined here as

$$\Delta\Phi(t) = \Phi_N(t) - \Phi_S(t) = -(\psi_N(t) - \psi_S(t)), \tag{12}$$

in which the guide phase in equation (5) cancels in the taking the difference. This phase increases with time when the northern period is shorter than the southern (as seen at the start of the interval in Figure 4c) and decreases with time when the southern period is shorter than the northern (as seen at the end of the interval). The beat period itself, the interval between successive times when the two systems are, e.g., in phase with each other, is given by

$$\tau_B(t) = \frac{360}{\left(\frac{\mathrm{d}}{\mathrm{d}t}(\Delta\Phi) \right)} = \frac{\tau_N \, \tau_S}{|\tau_N - \tau_S|}, \tag{13}$$

and is shown on a log scale in Figure 4d.

At the start of the interval the southern period was slightly longer than the northern by ~0.03–0.05 h (~2–3 min), as had been the case for much of the postequinox interval since late 2010 [*Provan et al.*, 2013, 2014]. While
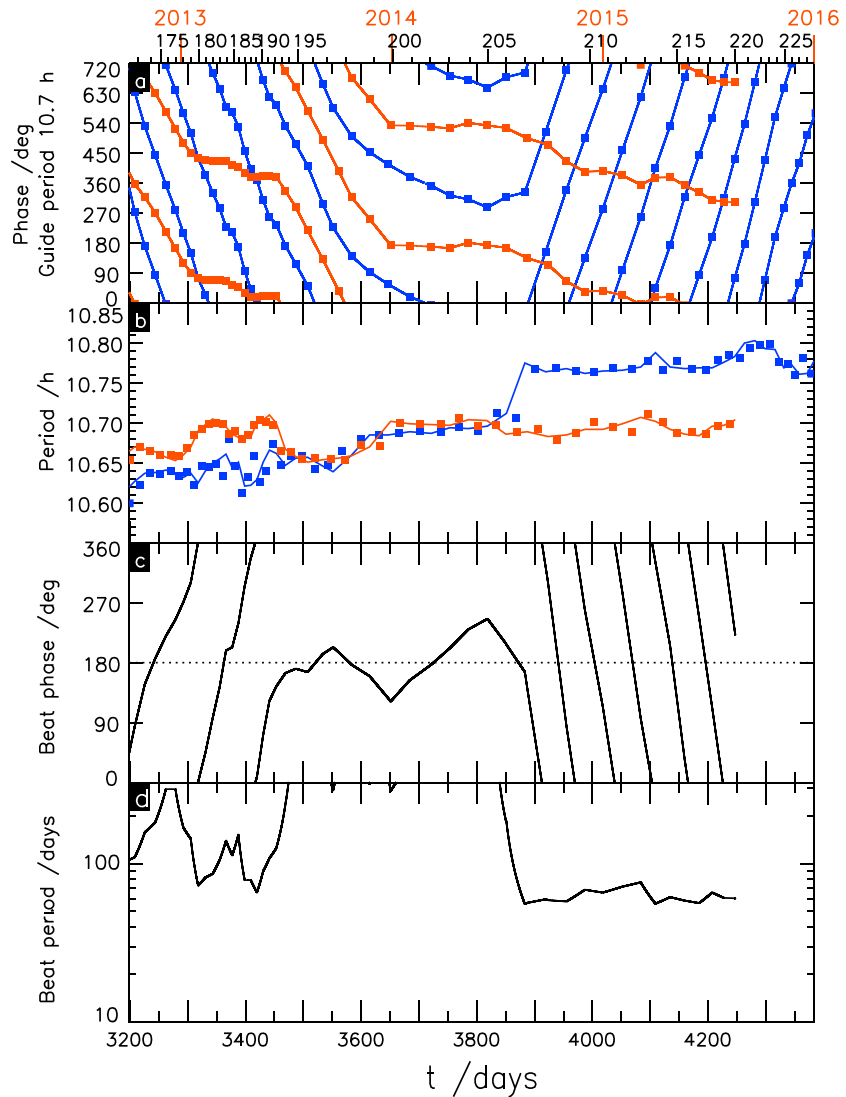
Figure 4. Summary plot of the magnetic field PPO phases and periods derived in Figure 3, shown over the same ~3 year study interval as in Figures 2 and 3. Year markers and Rev numbers are shown at the top of the plot as in Figures 2 and 3. (a) The northern (blue squares and lines) and southern (red squares and lines) PPO phases (degree) relative to a guide phase of fixed 10.70 h period, as in Figures 3a and 3c, respectively. (b) The two measures of the northern (blue data) and southern (red data) PPO periods (hour), as in Figures 3b and 3d. (c) The modulo 360° beat phase determined from the difference between the northern and southern magnetic phases (equation (12)), while (d) the beat period (days) (equation (13)) on a log scale, corresponding to the interval between successive times when the two systems are in phase with each other, or are in antiphase.

thus being closely comparable to the values deduced in these earlier studies in the interval of overlap to $t = 3510$ days, the higher-resolution magnetic periods determined here are initially seen to be quasi-oscillatory on a time scale which is comparable to the beat period of ~100 days (Figure 4d). These variations are such that the two periods move together when the two systems are near to antiphase, i.e., when $\Delta\Phi \sim 180°$ modulo 360° (Figure 4c), and move apart again when the two systems are near to in phase, i.e., when $\Delta\Phi \sim 0°/360°$ modulo 360° (see also Figure 4a). Two such cycles of behavior can be discerned initially, until on the third approach to antiphase conditions at ~3450 days, the two periods near coalesced at ~10.66 h to within uncertainties of ~0.005 h (~20 s). The more significant of these variations have previously been noted by Provan et al. [2013, 2014] in terms of the changes in period that occur at the end of their intervals E_4 and in F_1 and F_2. The present results show the relation of these variations to the beat phase, thus indicating their association with interhemispheric coupling of the two PPO systems as discussed in section 5.

Following their initial near coalescence, the two periods then remained very close to each other for more than a year, from ~3450 days (June 2013) to ~3850 days (July 2014), moving together to somewhat larger values ~10.70 h particularly during late 2013. Correspondingly, the phase difference between the two systems remained near antiphase during this interval (Figure 4c), varying around ~180° within limits of ~ ±45°, comparable to the expected uncertainties in the phase differences based on the phase uncertainty estimates discussed in section 2.3. We note from Figures 3a and 3c that these near-equal periods and near-constant phase differences were derived from entirely independent sets of northern and southern polar magnetic phase data (see Appendix A). Consideration of Figure 1 shows that the antiphase condition implies that the θ components of the two systems add to each other in the equatorial region, while the r and φ components subtract, as will also be discussed in section 5. This condition implies that the primary upward field-aligned currents of the two systems are located near the same LTs as each other as the systems rotate, as are the downward currents on the opposite side of the planet. A further implication is that the northern and southern SKR modulations should then be approximately in phase with each other, if the observed emissions correspond to sources at the same LTs in the two hemispheres, as will be shown to be the case in section 3.3.

Following the interval of near-coalesced periods, the northern period then increased to larger values ~10.77 h at around ~3900 days (September 2014) and remained at similar values to the end of the interval. The southern period, however, remained near ~10.70 h until it could no longer be discerned in the equatorial phase data after ~4250 days (September 2015). These data thus indicate that after ~3900 days the northern period shifted to enduringly longer periods than the southern by ~4–5 min, for the first time during the Cassini era.

As a consequence of the variations in northern and southern periods discussed above, the beat period in Figure 4 d oscillated around ~100 days during the initial interval when the southern system had a longer period than the northern by ~2–3 min but reduced to ~60 days during the later interval when the northern period had become longer than the southern by ~4–5 min. The value is mainly off-scale in the central interval of near-equal periods where the nominal beat period became comparable to or longer than the length of the data interval concerned, and hence not meaningful, the phase difference then being near constant with time as seen in Figure 4c.

2.5. North/South Amplitude Ratios Before and After Period Coalescence and Reversal
2.5.1. Precoalescence Amplitude Ratio
As indicated in section 2.3, the near-equatorial field data can be used to estimate the amplitude ratio of the northern and southern oscillations from the phase modulations caused by the superposition of the two signals [*Provan et al.*, 2011, 2013; *Andrews et al.*, 2012]. No models of PPO amplitudes in polar data, varying, e.g., with radial distance downtail, have yet been devised which would allow similar estimates from these data. As indicated in section 2.2, two sets of equatorial phase data were obtained during the present study interval, the first derived (principally) from unfiltered azimuthal field data on highly inclined orbits at the start of the interval from late 2012 to mid-2013 (Revs 173–194), and the second from filtered three-component data as the orbit returned to the equatorial plane at the end of the interval from early to late 2015 (Revs 211–221).

Figure 5 shows results for the first of these intervals, where Figures 5a and 5b show the (transformed) phase of the equatorial φ component (blue circles) relative to the north and south model phases derived from the independent sets of polar data. That is, in Figure 5a we show $((\psi_\varphi - 90°) - \psi_N)$, while in Figure 5b we show $((\psi_\varphi - 90°) - \psi_S)$. In Figure 5a the phase relative to the north phase increases near linearly with time between ~ −90° and ~ +90° over intervals of ~100 days and then switches by ~180° between these values, while in Figure 5b the phase relative to the south phase correspondingly falls between ~ +90° and ~ −90° over the same intervals, then also switches by ~180° between these values. This behavior is the characteristic signature of combined oscillations of near-equal amplitude modulated at a beat period of ~100 days (Figure 4d), in which zero crossings in the phase differences occur when the northern and southern systems are in phase, and 180° switches when they are in antiphase [*Provan et al.*, 2011, 2013; *Andrews et al.*, 2012; *Cowley et al.*, 2015]. Assuming for simplicity a fixed north/south amplitude ratio k during the interval, it can be shown that

$$\left(\psi_\varphi - 90°\right) - \psi_N = \tan^{-1}\left[\frac{(1/k)\sin\Delta\Phi}{1 + (1/k)\cos\Delta\Phi}\right], \qquad (14a)$$

and

$$\left(\psi_\varphi - 90°\right) - \psi_S = -\tan^{-1}\left[\frac{k\sin\Delta\Phi}{1 + k\cos\Delta\Phi}\right], \qquad (14b)$$
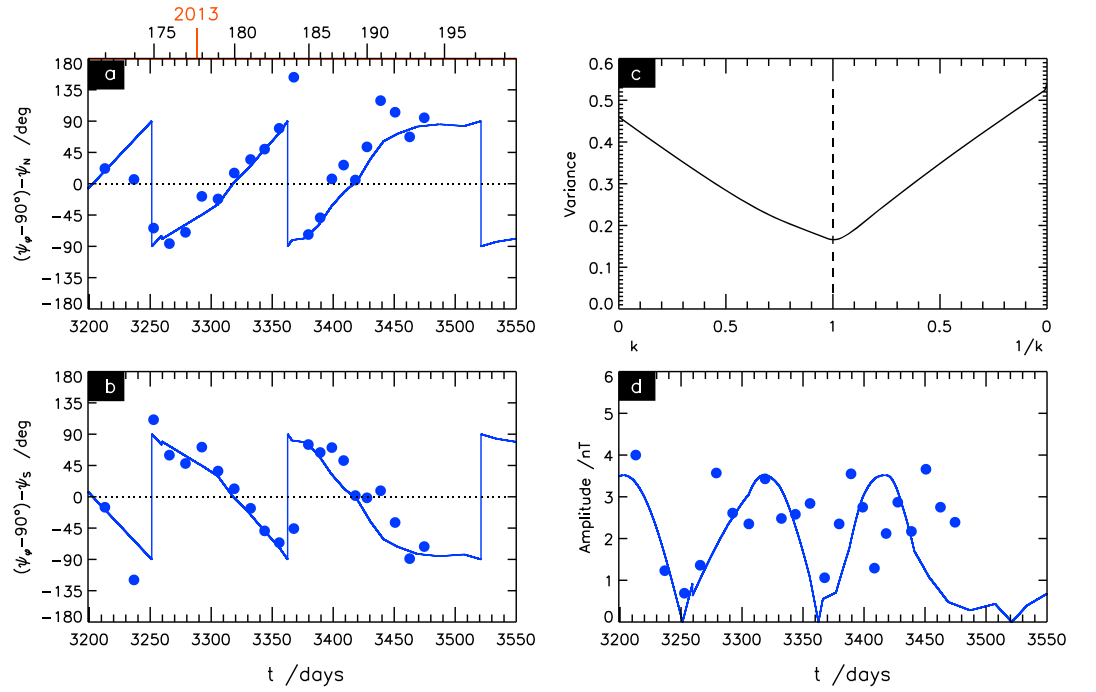
Figure 5. Analysis of PPO phase and amplitude data obtained from unfiltered equatorial azimuthal component data in late 2012 and early 2013. (a) The blue circles show transformed azimuthal phase data (90° subtracted to allow for lagging quadrature with the r component), relative to the northern PPO phase derived from northern polar data (Figure 3a). Year boundaries and Rev numbers are shown at the top of the figure in the same format as Figures 2–4. (b) The same data relative to the southern PPO phase derived from southern polar data (Figure 3c). The blue lines in both figures show the best fit model given by equations (14a) and (14b), based on the beat phase determined from the northern and southern polar data, and the best fit north/south amplitude ratio k. (c) The variance V between the data and the model (equation (7)) for k between zero and unity on the left, and for ($1/k$) between unity and zero (i.e., k between unity and infinity) on the right, showing a well-defined minimum at $k = 1.00$ (determined at steps in k and ($1/k$) of 0.01) marked by the vertical dashed line, which is the model displayed in Figures 5a and 5b. (d) The amplitude data (blue circles) and corresponding model (blue line) given by equation (15) using a best fit southern (and northern) amplitude of ~1.8 nT.

where $\Delta\Phi$ is the beat phase given by equation (12) [see, e.g., *Provan et al.*, 2013, equations (2b) and (2c)], and we note that the signs of the numerators and denominators are employed individually in the arctangents to define the angles over the full 360° range. The value of k can then be determined either by fitting equation (14a) to the data in Figure 5a or equation (14b) to the data in Figure 5b, these procedures being entirely equivalent since it can be shown that deviations of the data in Figure 5a from the model in equation (14a) are identical to the deviations of the data in Figure 5b from the model in equation (14b). Given the north and south phase models derived independently from the northern and southern polar data, amplitude ratio k is the only unknown. The fit is performed by determining the variance V between the data and the model (equation (7)) as k varies between zero and unity and then as ($1/k$) varies between unity and zero (i.e., as k varies between unity and infinity), at steps of 0.01 in both ranges. Results are shown in Figure 5c, where we see a clear minimum with $V \approx 0.17$ at $k = 1.00$, i.e., for closely near equal amplitudes. This minimum value of V implies an RMS deviation of the data from the model of ~35° (equation (10)). The model fit itself is shown by the blue lines in Figures 5a and 5b, which can be seen to provide a good overall description of the equatorial phase data.

Significant modulations should then also be present in the equatorial amplitudes, given by

$$B'_{0\varphi}(t) = B_{0\varphi\ S}\sqrt{1 + k^2 + 2k\cos\Delta\Phi}, \tag{15}$$

where $B_{0\varphi\ S}$ is the equatorial amplitude of the southern oscillation in the azimuthal field component, equal when $k = 1$ to the amplitude of the northern oscillation $B_{0\varphi\ N} = kB_{0\varphi\ S}$, and $B'_{0\varphi}(t)$ is the amplitude of the beat-modulated combined oscillation [e.g., *Provan et al.*, 2013, equation (2j)]. A least squares fit to the equatorial amplitude data to determine the best fit value of $B_{0\varphi\ S}$, the only unknown given k and the phase models, is shown in Figure 5d, where $B_{0\varphi\ S} = B_{0\varphi\ N} \approx 1.8$ nT. While the amplitude data are clearly quite

scattered, smallest values are indeed observed around the model zeros where the two systems are near antiphase, at ~3250 and ~3360 days. The correlation coefficient between the measured and model values is ~ +0.35. Very similar results were obtained by *Andrews et al.* [2012] from a previous interval during which equatorial data were obtained from unfiltered azimuthal component data on highly inclined orbits, in which clear modulations were also observed in the phases, but where the amplitudes were also rather scattered with a cross-correlation coefficient in that case of 0.28 (their interval D1 in 2008, see their Figure 9b). Overall, however, this analysis shows that the amplitudes of the two systems directly prior to the coalescence in periods were near equal in value. The analysis also provides a significant demonstration that the single oscillations observed independently in the northern and southern polar regions combine to produce dual-modulated oscillations in the equatorial region as recently emphasized by *Cowley et al.* [2016].

2.5.2. Postreversal Amplitude Ratio

Turning now to the second set of equatorial data obtained on near-equatorial orbits toward the end of the study interval, we recall that these were determined using filtered data from which the phases of all three field components can generally be determined. In this case we can apply the related procedure of examining the phase difference between the (r, φ) components and the θ component, which oscillates at the beat period about 0° for southern-dominated combined oscillations (i.e., for $k < 1$) and about 180° for northern-dominated combined oscillations (i.e., for $k > 1$). The advantage of this approach is that any "common jitter" in the phase values, i.e., short-term changes in phase in which all three field components vary together in a manner not described by the longer-term fitted phase models [e.g., *Provan et al.*, 2011], does not affect the results. The model modulation is given by

$$\Delta\psi_{r-\theta} = \psi_r - \psi_\theta = \left(\psi_\varphi - 90°\right) - \psi_\theta = -\tan^{-1}\left[\frac{2k\sin\Delta\Phi}{1 - k^2}\right], \qquad (16)$$

Where, again, the signs of the numerator and denominator in the arctangent on the right-hand side are taken individually to define the angle over the full 360° range [e.g., *Provan et al.*, 2013, equation (2g)]. We thus fit equation (16) to the phase difference data to determine k for the interval, given the north and south phase models shown in Figure 3 which define the beat phase $\Delta\Phi$. It is already apparent from the fact that these phase data are usually much more tightly grouped in N-format in Figure 3a than in S-format in Figure 3c that the northern oscillation is generally significantly stronger than the southern in this interval, i.e., that $k > 1$. It is further evident, however, that there is considerable variability in relative amplitude over the interval, including one set of phase measurements, for Rev 215, that has an almost pure southern polarization with θ in phase with the (transformed) φ phase, rather than being in antiphase. Nevertheless, making a fit of equation (16) to the overall phase difference data from Revs 211 to 220 (of which Rev 216 is missing due to a data gap, while Rev 219 does not return a reliable phase for the θ component) yields the results shown in Figure 6. Figure 6a shows the phase difference data, where the red circles correspond to $(\psi_r - \psi_\theta)$ and the blue to $((\psi_\varphi - 90°) - \psi_\theta)$, and where the discrepant nature of the data for Rev 215 is evident. The best fit model from equation (16), beat modulated with a period of ~60 days as indicated in Figure 4d, is shown by the black line for $(1/k) = 0.44$, i.e., for $k \approx 2.3$, corresponding to the variance minimum shown by the vertical dashed line in Figure 6b. The minimum value of V is ~0.21, corresponding to an RMS phase deviation between the model and the data of ~35°.

The best fit amplitude models are shown in Figure 6c, corresponding to a northern amplitude of ~0.8 nT for the r component, ~1.5 nT for θ, and ~1.4 nT for φ, with southern amplitudes that are then a factor ~2.3 less. However, the detailed agreement is seen to be very poor in this case, indicating a significant level of temporal amplitude variability in line with the above discussion, with correlation coefficients between the measured and model values of ~0.01 for the r component, ~0.01 for θ, and ~0.25 for φ. Overall, however, this analysis shows that in the interval following the period reversal the amplitude of the northern system had become dominant by a factor of more than 2 relative to the southern system, though with considerable variability being present. As discussed above, the lack of significant southern phase modulation in the equatorial data after ~4250 days indicates that the southern amplitude had further weakened to become less than ~20% of the northern, i.e., that by this time k had grown to become larger than ~5.

3. PPO Properties From SKR Data and Comparison With Magnetic Data

3.1. SKR Data Analysis Procedures

We now examine the PPO-related modulations observed in SKR emissions over the ~3 years of this study and compare the periods and phases derived from them with the periods and phases derived from the magnetic
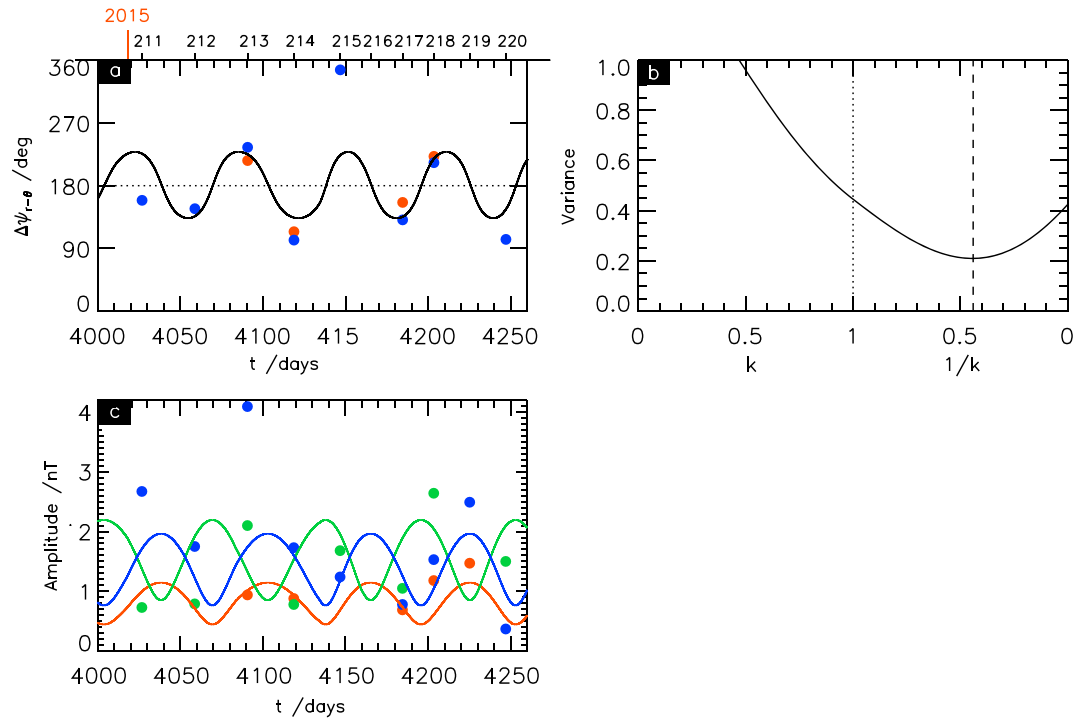
Figure 6. Analysis of PPO phase and amplitude data obtained from filtered equatorial field data in early and mid-2015, similar to Figure 5. (a) The phase differences $(\psi_r - \psi_\theta)$ (red circles) and $((\psi_\varphi - 90°) - \psi_\theta)$ (blue circles) versus time, together with the best fit model (black line) given by equation (16) based on the beat phase of the northern and southern phases determined from linear fits to the N- and S-format versions of these data shown in Figures 3a and 3c, and amplitude ratio k. (b) The variance V of the data from the model as a function of k in the same format as Figure 5c, with a well-defined minimum at $(1/k) = 0.44$ marked by the vertical dashed line, i.e., at north/south amplitude ratio $k \approx 2.27$, as therefore employed in Figure 6a. (c) The corresponding amplitude data, red, green, and blue for the r, θ, and φ field components, respectively, together with the best fit beat-modulated model given by equation (15) for best fit northern amplitudes of ~0.8, ~1.5, and ~1.4 nT, respectively. There is essentially no correlation between the data and model variations in this case.

field data in section 2. Analysis of the SKR data follows that described by *Lamy* [2011], in which emissions from the northern and Southern Hemispheres are identified on the joint bases of their sense of circular polarization and their latitudinal range of visibility. As indicated in section 1, SKR is emitted in the extraordinary (X) mode which is RH polarized in the Northern Hemisphere and LH polarized in the southern, with sources in one hemisphere illuminating the region down to ~20° latitude in the other [*Lamy et al.*, 2008a, 2008b; *Kimura et al.*, 2013]. RH emissions at latitudes greater than 20° south are thus taken to correspond to the Northern Hemisphere, while LH emissions at latitudes less than 20° north are taken to correspond to the Southern Hemisphere. The latitudinal selection is intended to exclude from the analyzed data set any nonnegligible ordinary (O) mode emissions at high latitudes (see discussion in *Lamy* [2011]). Polarization-separated SKR powers are integrated over the frequency interval 100–500 kHz, thus excluding narrowband emissions at lower frequencies, and inverse square normalized to a standard distance of one astronomical unit from the planet. Lomb-Scargle analysis of this quasi-continuous data set, specifically of the logarithm of the RH- and LH-normalized SKR powers, is then used to calculate normalized periodograms over a sliding 200 day window computed with 1 day resolution.

3.2. SKR PPO Periods and Initial Comparison With Magnetic Field Periods

Results are shown in Figure 7, where color-coded periodograms derived for periods between 10.5 and 10.9 h are plotted vertically, and shown versus time over the same interval as in Figures 2–4. Periodograms for the RH (northern) and LH (southern) emissions are shown in Figures 7a and 7c, respectively, which are repeated in Figures 7b and 7d with the corresponding SKR and magnetic field periods being overplotted as orange and white dotted lines, respectively. The dual panel format allows comparison of the derived SKR and magnetic field periods without relevant features in the SKR periodograms becoming obscured. The SKR periods have

been determined using iterative steps. The most prominent peak over the range 10.5–10.9 h was first extracted from periodograms of sufficiently high signal-to-noise ratio. The missing intervals were then completed by a search for the dominant peak over a restricted period range, aimed at favoring signal continuity for intervals where secondary maxima are significant, such as in the LH (southern) periodogram between ~3700 and ~4100 days. The magnetic field periods shown in Figure 7 correspond specifically to those determined directly from the linear fits to the phase data shown by the blue and red lines in Figures 3b and 3d, respectively, and in Figure 4b.

In Figure 7a it can be seen that a near-continuous peak occurs in the RH (northern) SKR periodograms which moves to longer periods with time, from ~10.64 h at the beginning of the interval to ~10.78 h at the end, which is taken to correspond to the northern SKR period shown by the orange dotted line overplotted in Figure 7b. This period can be seen to be generally in close agreement with that determined from the magnetic field data, shown by the white dotted line. However, a short gap in the continuity of the SKR peak occurs between ~3820 and ~3900 days, matching the interval where the magnetic data indicate the increase in northern period. When the peak resumes near ~3900 days the periodogram is noisier with significant secondary maxima. Over the subsequent interval the SKR period tracks the most prominent peak, while the magnetic period tracks a secondary maximum with a somewhat longer period that coalesces with the principal peak after ~4050 days. At this point the SKR and magnetic periods once more come into better agreement, then maintained to the end of the study interval. While reexamination of the magnetic phase data during this interval confirms evidence for the rapid and sustained increase in the northern period near ~3900 days not visible in the SKR data at this time (see discussion of Figure 9b in section 4 below), it is nevertheless the case that the behavior of the magnetic phases and hence periods is less well constrained than usual during this interval, due to the lengthy orbital period of ~30–40 days then prevailing (Figure 2e) and the consequent low cadence of the magnetic phase data set. Overall, however, both data sets agree that the northern PPO period increased significantly from values ~10.64 h in mid-2013, typical of most of the postequinox interval up to that time, to values ~10.78 h by mid-2015.

A near-continuous peak can similarly be traced in the southern periodograms in Figure 7c, taken to correspond to the southern SKR PPO period shown by the orange line in Figure 7d. This remains near periods of ~10.68–10.70 h, but weakens somewhat with time, and also exhibits some bifurcation signatures, e.g., 3650–3850 days and 4000–4150 days, which render the determination of the period somewhat uncertain during the central study interval. The tracked southern SKR period shown follows the most prominent and continuous of these peaks. Despite the difficulty in tracking the southern period after ~3700 days, however, the overall agreement with the southern magnetic field period overplotted in Figure 7d is seen to be excellent.

3.3. SKR PPO Phases and Initial Comparison With Magnetic Field Phases

The SKR periods determined from the periodograms in Figure 7 are compared in Figure 8a, where the blue line shows the northern (RH) period and the red line the southern (LH) period. These show slightly longer southern periods ~10.68 h than northern ~10.64 h at the start of the interval, followed by near coalescence at ~3500 days with joint period ~10.66 h rising to ~10.70 h by ~3800 days, and then gradual separation with the northern period increasing to ~10.79 h by the end of the interval while the southern period remained at ~10.70 h, in essential agreement with the magnetic periods shown in Figure 4b. These periods can then be integrated to determine a SKR phase $\Phi_{N,S}^*(t)$ which describes the times of sequential SKR maxima, conveniently defined to occur when $\Phi_{N,S}^*(t) = 360N\,\mathrm{deg}$ for successive integer N. Here SKR phases will be denoted by stars throughout. The constant of integration which defines the absolute value of the phase at time t (modulo 360°), and hence the actual times of SKR maxima, is determined by sinusoidal fits to the SKR power data organized by modulo 360° integrated SKR phase and time. Results are shown for the RH (northern) and LH (southern) emissions, respectively, in Figures 8b and 8c, where gray scaled SKR powers are plotted versus modulo 360° guide phase (vertically) and time (horizontally) over the same interval as in Figures 2–4. As for the magnetic field analysis, the guide phase corresponds to a fixed period of 10.70 h (equation (4a)), with two cycles of phase and repeated data being shown on the vertical axis to aid visualization of data continuity. Lighter grays indicate higher powers, while black intervals indicate times when SKR visibility conditions were not met for that sense of polarization, or other data gaps.
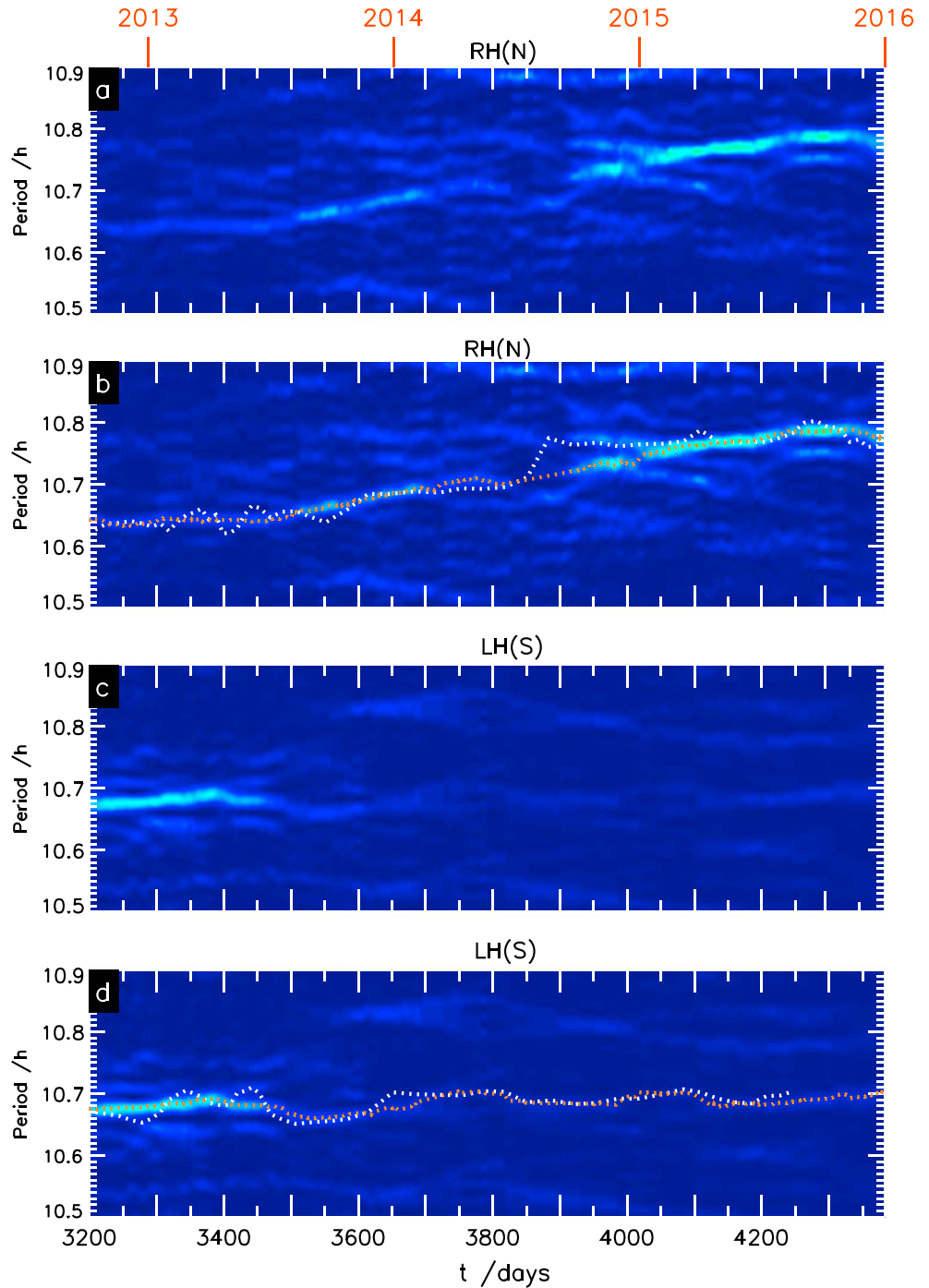
Figure 7. Color coded periodograms derived by Lomb-Scargle analysis of integrated SKR power data for periods between 10.5 and 10.9 h are shown plotted versus time over the same ~3 year interval as in Figures 2–4, with PPO periods overplotted. (a) RH circular polarized emissions observed at latitudes above 20° south, corresponding to northern emissions, while (c) LH circular polarized emissions observed at latitudes below 20° north, corresponding to southern emissions. (b and d) The data are repeated, while overplotted we show the corresponding northern and southern periods, respectively, determined from the near-continuous maxima in these data (orange dotted lines), and from the magnetic field results in Figures 3b and 3d (white dotted lines), specifically the blue and red lines in those figures.

The blue line in Figure 8b and the red line in Figure 8c show the SKR phases $\psi^*_{N,S}(t)$ relative to the guide phase, which can be seen to trace through the power peaks in the RH-modulated (northern) and LH-modulated (southern) emissions, respectively, thus providing support for the SKR periods shown in Figure 7. Analogously to the magnetic phases given by equation (5), the SKR phases are given by

$$\Phi^*_{N,S}(t) = \Phi_g(t) - \psi^*_{N,S}(t) = \frac{360\,t}{\tau_g} - \psi^*_{N,S}(t), \tag{17}$$

where the second expression on the right-hand side is valid for a guide phase of fixed period τ_g, such that by construction SKR maxima occur when the guide phase is equal to $\psi^*_{N,S}(t)$ modulo 360°. For the RH (northern) emissions in Figure 8b, the data and modulations are sufficiently continuous to define the northern SKR phase over the whole study interval. For the LH (southern) emissions in Figure 8c, however, the data are sufficiently discontinuous in the central interval that a reliable overall phase cannot be determined. In this case we have calculated the phase separately in two intervals on either side, from the start of the study interval to $t = 3675$ days, and from $t = 4100$ days to the end of the study interval, as shown by the solid red line segments. In the central interval between these times we have instead determined individual modulo 360° phase values from sinusoidal fits to the LH powers integrated over each interval of continuous measurements, shown by triangles joined by dotted lines. Since these intervals are much shorter than the 200 day sliding data windows employed to determine the phases more generally, these values are expected to provide only approximate measures of the southern phase during this interval.

The red dashed line and triangles in Figure 8b and the blue dashed line in Figure 8c then show the LH (southern) phase overplotted on the RH (northern) data, and vice versa. These demonstrate that during the interval of coalesced SKR periods in Figure 8a between ~3500 and ~3800 days, indicative of a near-constant phase relationship between the northern and southern SKR modulations, the two systems, in fact, approach in-phase conditions, closely so during the interval to ~3675 days where both phases are determined from 200 day sliding data windows, and more approximately thereafter to ~3800 days where the southern phases are indicated by the triangles. We recall from section 2.4 that the magnetic systems came into near antiphase during this interval, such that in-phase SKR modulations were anticipated on the basis of the picture shown in Figure 1, as now confirmed here.

To investigate the relationship between the SKR and magnetic field phases, and hence the orientation of the perturbation field and current system at times of SKR maxima, in Figures 8d and 8e we have reproduced the RH (northern) and LH (southern) SKR power data and phases from Figures 8b and 8c, respectively, and have overplotted the corresponding magnetic phases. Specifically, the blue squares joined by solid lines in Figure 8c show the northern magnetic phase $\psi_N(t)$ from Figure 3a, while the red squares joined by solid lines in Figure 8e show the southern magnetic phases $\psi_S(t)$ from Figure 3c. Apart from the interval between ~3875 and ~4050 days when the northern periods deduced from the SKR and magnetic data differ significantly as seen in Figure 7b, it can be seen in Figure 8d that the northern SKR and magnetic phases are to a first approximation in phase with each other, such that the magnetic phase also lies approximately along northern (RH) SKR maxima. This means that at times of northern SKR maxima, $\Phi^*_N \approx 0°$ modulo 360°, the quasi-uniform field of the northern system is directed approximately sunward, $\Phi_N \approx 0°$ modulo 360°, such that the upward field-aligned current of the northern system is located near dawn (Figure 1a). Similarly, it can be seen in Figure 8e that the southern SKR and magnetic phases are to a first approximation in antiphase with each other, such that the magnetic phase lies approximately along southern (LH) SKR minima. This means that at times of southern SKR maxima, $\Phi^*_S \approx 0°$ modulo 360°, the quasi-uniform field of the southern system is directed approximately antisunward, $\Phi_S \approx 180°$ modulo 360°, such that the upward field-aligned current of the southern system is then also located near dawn (Figure 1c). In following section 4 we provide a more precise discussion of these phase relationships.

4. Further Comparison of SKR and Magnetic Field Periods and Phases

In Figure 9 we provide a more detailed comparison of the periods and phases derived from the SKR and magnetic field measurements. Figure 9a compares the northern (blue) and southern (red) periods determined from both the magnetic field (lines and squares) and SKR data (dashed lines), as previously shown individually in Figures 4b and 8a. As previously indicated in the discussion of Figure 7 in section 3.2, the overall agreement
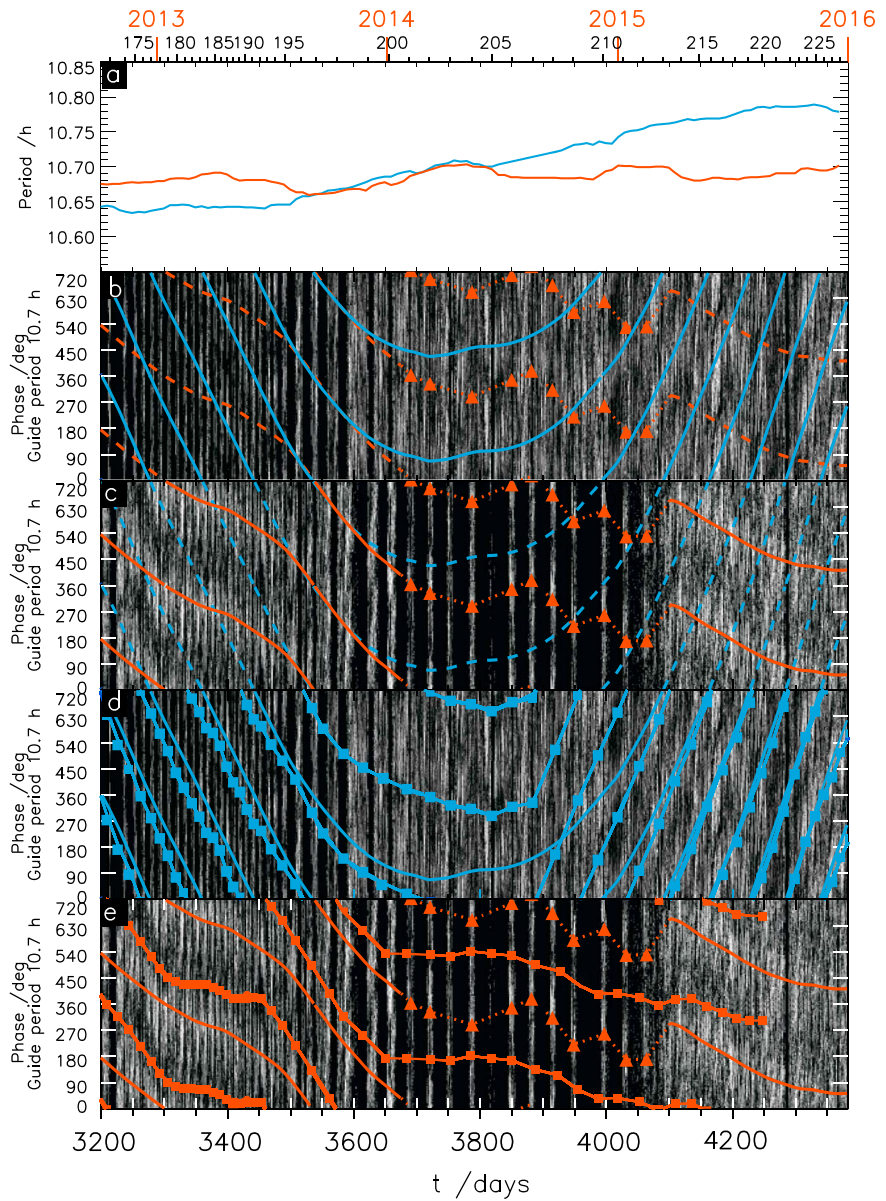
Figure 8. Plots showing SKR periods and integrated phases over the same ~3 year interval as in Figures 2–4 and 7, with Rev markers and year boundaries being shown at the top of the plot as in Figures 2–4. (a) The SKR periods versus time from Figure 7, where the blue line shows the RH (northern) period from Figure 7b, and the red line the LH (southern) period from Figure 7d. (b–e) Gray scaled SKR powers plotted versus modulo 360° guide phase vertically, showing two cycles with repeated data, and time horizontally, where, as in Figures 3 and 4, the guide phase corresponds to a fixed period of 10.70 h with value zero at time zero (00 UT on 1 January 2004). Lighter grays correspond to higher SKR powers, with intervals where corresponding SKR visibility conditions were not met being shown black, as are other data gaps. Figure 8b corresponds to RH (northern) SKR emissions where the overplotted blue line indicates the northern SKR phase marking the location of the northern SKR power maxima, obtained by integration of the northern SKR period in Figure 7b followed by fitting to these data. The red dashed line and triangles show the corresponding phase for the LH (southern) data. Figure 8c similarly corresponds to LH (southern) SKR emissions, where the red lines indicate the southern SKR phase marking the southern SKR power maxima, and the blue dashed line the northern phase from Figure 8b. In this case the southern SKR phase has been determined from separate integration of the periods shown in Figure 7d over the intervals before 3675 days and after 4100 days followed by fitting to these data, while the triangles joined by dotted lines show approximate phases determined from sinusoidal fits to the LH powers integrated over each of the short intervals of continuous measurements shown in the plot. In Figures 8d and 8e we reproduce the RH (northern) power and phase and the LH (southern) power and phase from Figures 8b and 8c, respectively, but now overplot the corresponding magnetic field phases from Figure 3. Specifically, the blue squares and lines in Figure 8d correspond to the northern magnetic phase model shown in Figure 3a, while the red squares and lines in Figure 8e correspond to the southern magnetic phase model shown in Figure 3c.
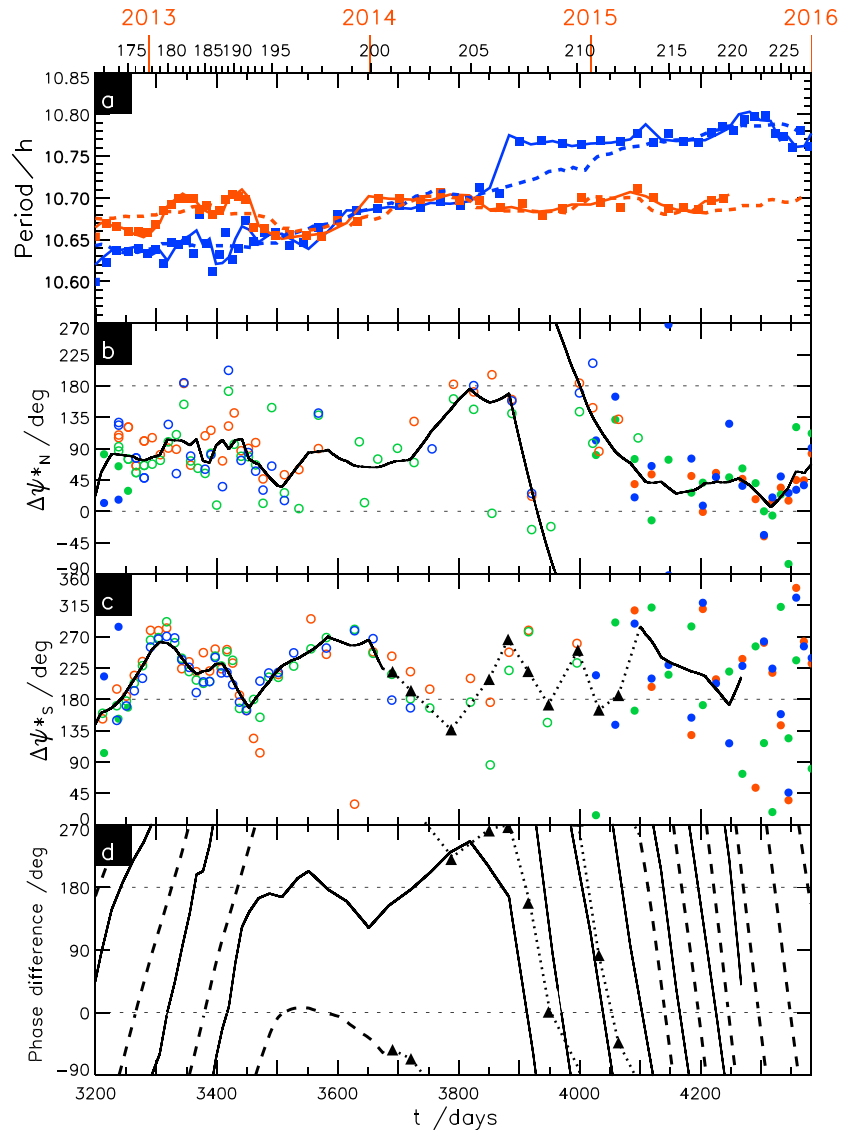
Figure 9. Comparison of SKR and magnetic field periods and phases shown in Figure 7 and 8, over the same interval as previous figures. Rev numbers and year boundaries are shown at the top of the plot. (a) The northern (blue) and southern (red) periods derived from SKR (dashed lines) and magnetic field data (solid lines and squares), respectively. The SKR periods are derived from the periodograms shown in Figures 7, while the magnetic periods are those shown in Figure 3. (b) The phase difference between the northern SKR and magnetic field phases $\Delta\psi_N^*(t)$, SKR minus magnetic in Figure 8a (equation (18a)), together with the Rev-by-Rev magnetic phase data from which the magnetic phases were derived, in the same format as Figure 3a. (c) The phase difference between the southern SKR and magnetic field phases $\Delta\psi_S^*(t)$, SKR minus magnetic in Figure 8b, together with the Rev-by-Rev magnetic phase data from which these magnetic phases were derived, in the same format as in Figure 3c. (d) The phase difference between the northern and southern modulations for both the magnetic $\Delta\Phi$ (equation (12)) and the SKR $\Delta\Phi^*$ phase data (equation (19)).

between the SKR and magnetic field periods is good, though the SKR values do not reproduce all of the shorter-term variations in the magnetic periods, due to differences in the length of the data intervals employed. In the interval prior to period coalescence, for example, the magnetic periods were determined over intervals of ~50 days of phase data corresponding to 5 Revs (see Figure 2e), compared with the standard 200 day data window for the SKR periods. Corresponding analysis of magnetic data with a 200 day data window (not shown) produces similar results to those determined from the SKR data in this interval. However, both analyses confirm the coalescence of the two periods in mid-2013, together with a separation in mid-2014 leading to an enduring reversal in periods northern longer than southern at that time, even though the magnetic data indicate a fairly abrupt separation, while the SKR data suggest a gradual evolution.

In Figures 9b and 9c we examine the differences between the SKR and magnetic field phases for the northern and southern systems seen Figures 8a and 8b, respectively. These differences are defined as

$$\Delta\psi_{N,S}^*(t) = \psi_{N,S}^*(t) - \psi_{N,S}(t) = \Phi_{N,S}(t) - \Phi_{N,S}^*(t), \tag{18a}$$

i.e., the difference between the SKR and magnetic phase values shown by the blue and red lines in Figures 8d and 8e, where in the second form on the right-hand side we have used equations (5) and (17) and the common guide phase $\Phi_g(t)$ has dropped out in taking the difference. Since $\Phi_{N,S}^*(t) = 0°$ (modulo 360°) at the times of corresponding SKR maxima, we can also write (to modulo 360°)

$$\Delta\psi_{N,S}^*(t) = \psi_{N,S}^*(t) - \psi_{N,S}(t) = \Phi_{N,S\ max}(t), \tag{18b}$$

where $\Phi_{N,S\ max}(t)$ is the value of the magnetic phase at times of corresponding SKR maxima. Since the magnetic field phases $\Phi_{N,S}(t)$ define the orientation of the equatorial quasi-uniform perturbation field with respect to noon at any time (i.e., the orientation with respect to noon of the $\Psi_{N,S} = 0°$ meridians in Figure 1), the phase differences $\Delta\psi_{N,S}^*(t)$ thus give the orientation with respect to noon of the northern and southern quasi-uniform fields at the times of corresponding SKR maxima and hence also the LTs of the related upward field-aligned currents. According to Figure 1, the upward field-aligned current of the northern system in the Northern Hemisphere lags by ~90° in azimuth relative to the northern quasi-uniform equatorial field (i.e., is located ~6 h LT earlier), while the upward field-aligned current of the southern system in the Southern Hemisphere leads by ~90° in azimuth relative to the southern quasi-uniform equatorial field (i.e., is located ~6 h LT later).

The northern phase difference $\Delta\psi_N^*(t)$ is shown in Figure 9b together with the N-format Rev-by-Rev magnetic phase data that define the northern magnetic phase (Figure 3a). In the initial interval to ~3750 days the phase difference is seen to vary by a few tens of degrees about ~90°, showing that the quasi-uniform field of the northern system was directed toward dusk at northern SKR maxima, with the northern upward field-aligned current thus located near noon. During the later interval beyond ~4050 days when the SKR and magnetic field periods were once again in agreement, the phase difference was modestly reduced to values ~30°, implying that the uniform field of the northern system was directed toward ~14 h LT at northern SKR maxima, with the northern upward field-aligned current being located at ~8 h LT in the postdawn sector. These data are thus indicative of the dominance of postdawn to noon sources during these intervals. In the interval between these times when the northern SKR and magnetic field periods are not in agreement, phase difference $\Delta\psi_N^*(t)$ is seen in Figure 9b to rotate rapidly through more than ~360°, showing that the difference in northern SKR and magnetic field periods in Figure 9a integrates to a phase difference corresponding to somewhat more than one whole rotation of the northern system in a total number over the interval of disagreement of ~500. To avoid most of this discrepancy, the magnetic phase values determined prior to ~3900 days would have to be joined directly to those observed after ~4000 days without inclusion of the ~360° relative phase variation. However, this would ignore the magnetic phase behavior observed in the interval between these times, essentially the phase values for Revs 207–209, which contain the evidence in the magnetic phase data for the rapid increase in the northern period at this time, together with the subsequent falling relative phases between ~4000 and 4100 days. Alternatively, we may instead propose that following the sudden decrease in $\Delta\psi_N^*(t)$ between ~3900 and ~3950 days as shown in Figure 9b, the phase difference then increased equally sharply between ~3950 and ~4000 days to join the curve again as shown, this implying a transient decrease in period by ~0.05 h during the interval relative to that inferred from the SKR data. In this interpretation, the transition to longer northern periods in the magnetic data would thus begin with a large ~100 day oscillation of the northern period of ~0.1 h peak-to-peak about the northern SKR values, this variation remaining unresolved in the SKR data (similar to the interval prior to ~3500 days). However, due to the low cadence of the magnetic phase data during this interval, no intermediate values are available that would support or discriminate between these scenarios. While the northern SKR power data shown in Figure 8d are somewhat noisy during the interval between ~3900 and ~4000 days, we note that they are better organized by the northern SKR phase than the northern magnetic phase in the subsequent interval to ~4100 days where discrepancies in the period remain. It thus remains unclear how these discrepancies may be resolved given the limitations of the data and the analysis protocols employed. Nevertheless, we reiterate our view that it is physically impossible for the magnetic field and SKR periods to actually be significantly different during this (or any other) interval and note that both data sets support the central conclusion that starting in mid-2014 the northern PPO period increased to significantly longer periods than hitherto observed during the Cassini mission.

The southern phase difference $\Delta\psi_S^*(t)$ is shown in Figure 9c together with the S-format Rev-by-Rev magnetic data that define the southern magnetic phase (Figure 3c). These values can be seen to vary by several tens of degrees about ~225° over the whole interval for which southern magnetic phases are defined (up to ~4250 days), with the well-defined deviations around that value in the initial interval up to ~3500 days being related to the ~100 day variations in the magnetic phases and periods discussed in section 2.4. These variations aside, the implication of these results is that the quasi-uniform field of the southern system pointed consistently postmidnight at times of southern SKR maxima, such that the associated southern upward field-aligned current region based on Figure 1 and implied SKR sources were located postdawn.

Short intervals of disagreement aside, therefore, these results indicate that the northern and southern SKR emissions observed throughout the study interval were responding principally to dominant northern and southern sources in the postdawn sector [*Lamy et al.*, 2009], similar to the situation throughout the preequinox interval reported previously [*Andrews et al.*, 2008, 2010b, 2012; *Provan et al.*, 2011]. This is certainly not surprising in the later part of the interval after ~4100 days, when the spacecraft orbit had become near equatorial with apoapsis located in the predawn sector (Figures 2b and 2d), where strobe-like modulations due to the dominant dawn sources at ~8 h LT are expected to prevail [*Andrews et al.*, 2011]. Indeed, taking the average of the phase difference data after 4100 days shown by the black lines in Figures 9b and 9c yields values of 36° ± 12° for the northern data and 221° ± 28° for the southern, indicating that at times of northern SKR maxima the quasi-uniform field of the northern system pointed toward 14.4 ± 0.8 h LT, while at times of southern SKR maxima the quasi-uniform field of the southern system pointed toward 2.7 ± 1.8 h LT. These averages and standard deviations were determined using directional statistics methods as outlined in section 4.3 of *Andrews et al.* [2012]. The implied LTs of the upward field-aligned currents and SKR sources at these times are thus ~8 h for the northern system and ~9 h for the southern, in close agreement with the expectations discussed in section 2.2.

During the earlier part of the interval up to ~3475 days, however, apoapsis, where the spacecraft spends most time, was instead located in the postnoon sector, before rotating via midnight into the dawn sector (Figure 2d). For near-equatorial observations in this sector the principal visible SKR sources are instead expected to be located near noon with the northern and southern quasi-uniform fields pointing toward dusk and dawn, respectively, at corresponding SKR maxima [*Andrews et al.*, 2011], as indeed reported under these circumstances by *Andrews et al.* [2012]. However, these earlier observations were obtained in the present study on highly inclined orbits for which no simple SKR source visibility model has yet been devised, with results that nevertheless suggest that the principal sources visible in the Northern Hemisphere were indeed located near noon, while the principal sources visible in the Southern Hemisphere remained located in the postdawn sector. More precisely, taking the average of the phase difference data prior to 3475 days shown by the black lines in Figures 9b and 9c yields values of 84° ± 15° for the northern data and 212° ± 32° for the southern, meaning that at times of northern SKR maxima the quasi-uniform field of the northern system pointed toward 17.6 ± 1.0 h LT, while at times of southern SKR maxima the quasi-uniform field of the southern system pointed toward 2.1 ± 2.1 h LT. The implied locations of the upward field-aligned currents and SKR sources at these times are thus ~12 h LT for the northern system and ~8 h LT for the southern, though we note the significantly large ranges in the above LT values. These values are in close agreement with the prior results of *Provan et al.* [2014] and *Cowley and Provan* [2016] during the overlapping intervals of these studies (see their Figures 7d and 5b, respectively).

We further note that the phase differences and implied source locations remained at similar values during the subsequent interval between ~3475 and ~3650 days while apoapsis rotated via midnight into the dawn sector (Figure 2d). Near-equatorial observations in this sector would be expected to respond to sources in the midnight to predawn sector, such that the northern phase difference in Figure 9b would be expected to lie in the range ~270°–315° during this interval (quasi-uniform field of the northern system pointing in the dawn to postdawn sector at northern SKR maxima), while the southern phase difference in Figure 9c would be expected to lie in the range ~90°–135° (quasi-uniform field of the southern system pointing in the dusk to postdusk sector at southern SKR maxima). However, no such changes in the relative phase are seen in Figure 9b or 9c, indicating instead that sources in the postdawn to noon sector remained dominant on the relevant segments of these highly inclined orbits.

In Figure 9d we compare the difference in phase between northern and southern systems as given by equation (12) for the magnetic phase difference (the beat phase $\Delta\Phi(t)$) and correspondingly for the SKR phase difference by

$$\Delta\Phi^*(t) = \Phi_N^*(t) - \Phi_S^*(t) = -\left(\psi_N^*(t) - \psi_S^*(t)\right). \tag{19}$$

In general, if the observed northern and southern SKR emissions are responding to sources centered at azimuths $\varphi_{N,S}^*$ in the two hemispheres, and if power maxima occur when the corresponding upward field-aligned currents of the two systems are located at these azimuths, such that from Figure 1 we have

$$\Phi_{N\ max} \approx \varphi_N^* + 90° \tag{20a}$$

and

$$\Phi_{S\ max} \approx \varphi_S^* - 90°, \tag{20b}$$

then substitution into equation (18b) followed by subtraction of the southern phase difference $\Delta\psi_S^*(t)$ from the northern phase difference $\Delta\psi_N^*(t)$ yields

$$\delta(\Delta\Phi) = \Delta\Phi - \Delta\Phi^* = 180° + \left(\varphi_N^* - \varphi_S^*\right). \tag{21}$$

Thus, if the effective azimuths of the two hemispheric SKR sources are approximately equal, as will generally be the case at least for near-equatorial observations, the magnetic field and SKR "beat" phases should be approximately in antiphase. In Figure 9d, where the magnetic phase difference $\Delta\Phi$ is shown by the solid line (as in Figure 4c) and the SKR phase difference $\Delta\Phi^*$ by the dashed lines and triangles, this is seen to be approximately the case for much of the study interval, specifically from the start of the interval to $t \approx 3700$ days and from $t \approx 4100$ days to the end of the interval. In the earlier of these intervals the effect of the ~50° difference in north and south source azimuths noted above is nevertheless apparent as a modest shift in $\delta(\Delta\Phi)$ away from antiphase. When the northern and southern periods near coalesce after ~3500 days with the magnetic systems in antiphase, $\Delta\Phi \approx 180°$ modulo 360°, the two SKR modulations then closely approach in-phase conditions $\Delta\Phi^* \approx 0°$ modulo 360° as anticipated in section 2.4 (as also seen in Figures 8b and 8c), at least initially up to $t \approx 3700$ days. In the immediately following interval when the southern SKR phase is less well defined and indicated approximately by the triangles, however, $\delta(\Delta\Phi)$ moves toward quadrature and even to in-phase conditions. Further major departures from the antiphase condition in $\delta(\Delta\Phi)$ also occur in the short interval when the northern SKR and magnetic field periods do not agree with each other, but as noted above the difference returns close to antiphase again when the periods come back into agreement after ~4100 days.

5. Summary and Discussion

Previous studies of the PPO oscillations in Saturn's magnetosphere using Cassini magnetic and SKR data have shown that during southern summer the two PPO periods were separated by ~12–14 min, ~10.8 h for the dominant southern oscillation, and ~10.6 h for the northern but converged to a near-common value of ~10.7 h over a ~2 year interval centered near vernal equinox in August 2009 [*Gurnett et al.*, 2010, 2011; *Lamy*, 2011; *Andrews et al.*, 2012]. Following brief near coalescence, the data further indicate that the periods then separated again with the southern ~10.69 h remaining longer than the northern ~10.64 h, but now by only ~2–4 min [*Provan et al.*, 2013, 2014]. These conditions persisted for the following ~3 years to mid-2013, but with the oscillations undergoing abrupt changes in relative amplitude at intervals of ~100–200 days between southern dominance, northern dominance, and near-equal amplitudes, with small abrupt changes in the periods occurring at the same time. In the present paper we have examined the oscillations in both magnetic and SKR data over the ~3 year interval from late 2012 to the end of 2015, thus modestly overlapping with the study by *Provan et al.* [2014], spanning from ~3 years after vernal equinox to ~1.5 years before northern solstice in May 2017.

The magnetic field results show that toward the end of 2012 the closely separated periods became weakly modulated at the beat period, moving together when the two systems were near antiphase and apart when near in phase, until they near coalesced in antiphase at a common period of ~10.66 h in mid-2013, directly after the end of the interval studied by *Provan et al.* [2014]. The two periods then remained in that condition within magnetic measurement uncertainties of ~20 s, and SKR measurement uncertainties of ~30–40 s, for

the following year to mid-2014, drifting slowly together to longer periods of ~10.70 h over the interval. These conditions were deduced using magnetic phase measurements obtained independently in the northern and southern magnetospheric polar regions on highly inclined Cassini orbits, together with SKR data hemispherically separated using both emission polarization and latitude constraints. In mid-2014 the northern oscillations continued to increase to longer periods, reaching ~10.78 h by the end of 2015, while the southern period remained near ~10.70 h. Both magnetic and SKR data after mid-2014 thus confirm the occurrence of the first Cassini era enduring reversal in PPO periods, northern period longer than southern by up to ~5 min, which took place ~5 years after vernal equinox and ~3 years before northern solstice. However, while the magnetic data suggest a somewhat sudden increase in the northern period after mid-2014, the SKR data indicate a gradual evolution to closely similar periods after the beginning of 2015. Analysis of available equatorial magnetic data shows that the northern and southern amplitudes were near equal in the interval immediately prior to coalescence in mid-2013, in agreement with the results of *Provan et al.* [2014], but that the northern oscillations became increasingly dominant in the interval of reversed periods after the beginning of 2015. Due to orbit constraints, no equatorial data are available in the intervening interval from which the relative amplitudes could be determined. The relative phasing between the magnetic oscillations and the SKR modulations indicates that the observed emissions were dominated by SKR sources in the postdawn to noon sector throughout, despite the somewhat variable nature of the Cassini orbit.

We now consider some physical implications of these results, beginning with the observation of near coalescence of the northern and southern PPO periods in antiphase for the 1 year interval between mid-2013 and mid-2014, immediately prior to the enduring reversal. The coalescence took place via a small increase in the northern period and a simultaneous small decrease in the southern period to commonality (within ~20 s for the magnetic measurements), following (at least) two previous near-coalescence events that occurred as the northern and southern magnetic phases approached the antiphase condition. After coalescence the two periods tracked each other over the following year as the joint period increased from ~10.66 to ~10.70 h (Figure 9a). This behavior suggests the presence of weak interhemispheric coupling of the two systems that maintained commonality of the periods in antiphase during this interval. The weakness of the coupling is suggested by the fact that the two systems remained at closely spaced (~2–4 min) but clearly separated periods for around three postequinox years before eventually falling into step with each other in mid-2013. The total deviation in magnetic phase from antiphase over the 1 year interval was no more than ~45° (Figure 4c) comparable to the phase difference uncertainties, which implies a difference in the mean periods of the two systems over the interval (in the sense of section 3.3 of *Cowley and Provan* [2016]) of no more than ~6 s, or ~0.01%.

The combined PPO system formed during coalescence is illustrated in Figure 10, in a similar format to Figure 1. The current system is sketched in the $\Psi_{N,S} = 90° - 270°$ meridian in Figure 10a and has upward and downward field-aligned currents located at the same LT in the two hemispheres, closing principally through the central region of the magnetosphere, thereby producing a common rotating force on the plasma. The associated perturbation fields are shown in the $\Psi_{N,S} = 0° - 180°$ meridian in Figure 10b, corresponding to Figure 10a viewed from the left, and are such that the quasi-uniform (r, ϕ component) fields in the equatorial region tend to cancel each other, while the colatitudinal fields add, connecting the perturbation fields of the two systems from pole to pole. While we do not know for certain the relative strengths of the two systems during this interval, our results show that the two amplitudes were closely comparable in the immediately prior interval (section 2.5.1), which is the condition illustrated here. Under these antiphase conditions the thermospheric and ionospheric twin-vortex flows which drive the currents and perturbation fields flow in the same sense as each other in the two ionospheres, out of the plane of the diagram in Figure 10a in both polar regions, reversing to into the plane of the diagram in the regions equatorward of the principal field-aligned current sheets in both hemispheres [e.g., *Jia et al.*, 2012; *Jia and Kivelson*, 2012; *Southwood and Cowley*, 2014; *Hunt et al.*, 2014, 2015]. The flow driven from one ionosphere will generally exert a drag force on the other ionosphere, at least in the region of outer closed field lines where the principal PPO-related field-aligned currents flow [*Hunt et al.*, 2014, 2015], thus tending in this relative phase condition to reinforce the two flows. These flows also combine to drive associated rotating twin-vortex flows within the magnetosphere via the above force, thus giving rise to, e.g., the "plasma cam" effect described by *Burch et al.* [2009]. The consequent in-phase condition of the field-aligned currents (with respect to the ionosphere) in the two hemispheres also results in approximately in-phase modulations of the northern and southern SKR emissions,
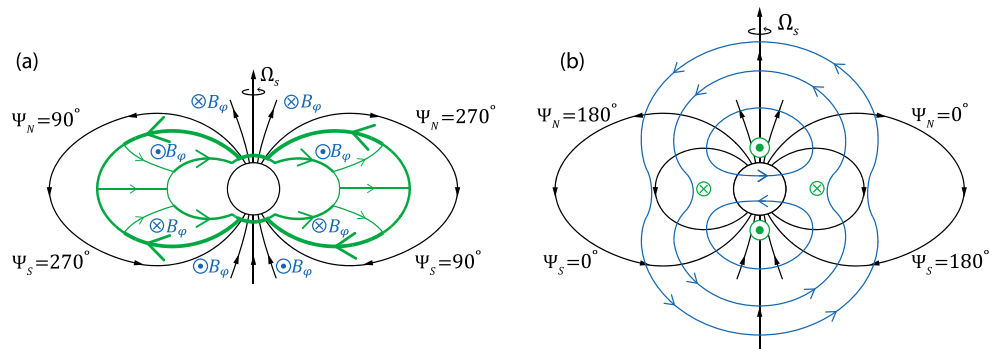
Figure 10. Sketches showing the electric currents and perturbation fields of the antiphase northern and southern PPO systems during the interval of near-coalesced periods between mid-2013 and mid-2014, in a format similar to Figure 1. Green arrowed lines and symbols indicate electric currents, blue arrowed lines and symbols indicate the associated perturbation magnetic fields, while black arrowed lines show the background magnetospheric magnetic field. Circled dots and crosses show vectors pointing out of and into the plane of the figure, respectively. (a) principally shows the currents in the $\Psi_{N,S} = 90° - 270°$ meridian plane, while (b) principally shows the perturbation fields in the $\Psi_{N,S} = 0° - 180°$ meridian plane, corresponding to Figure 10a viewed from the left. With increasing time this system of current and perturbation field rotates around the vertical axis with the period of the coupled northern and southern PPOs.

as observed. In the opposite magnetic in-phase condition the two flow systems would instead be opposed, the drag force of one tending to diminish the effect of the other. Furthermore, under the condition where the two systems are not phase locked but have slightly differing periods, such as during the early months of the present study interval, simple considerations show that the effect of an interhemispheric drag is such that the periods will move together toward a common value when the two magnetic systems approach antiphase in the beat cycle, with the flow systems, field-aligned currents, and SKR modulations in phase, and move apart when the two magnetic systems are in phase in the beat cycle, with the flow systems, field-aligned currents, and SKR modulations in antiphase. This picture is in approximate conformity with the behavior determined here in the interval leading up to period coalescence, in which two cycles of such beat-modulated period oscillations were observed in the magnetic field data before near coalescence occurred on the third approach to magnetic antiphase in mid-2013 (Figures 4 and 9).

Turning now to the reversal in periods after mid-2014, we note that the increase in the northern period to ~10.78 h by the end of 2015 brings its value close to that of the southern period observed during southern solstice conditions between a half and a quarter of a Saturn year earlier, while the southern period, remaining at ~10.70 h, had not decreased to values comparable to the northern period during southern solstice. This is shown in Figure 11, where we plot a compendium of PPO periods and related data over a full Saturn year (~29.5 Earth years) from the last northern solstice in mid-December 1987 to the next in late May 2017. In Figure 11a we show the latitude of the Sun at Saturn, where solstices and equinoxes are marked at the top of the figure and indicated by the vertical dotted lines, while in Figure 11b we plot the daily sunspot number indicative of solar cycle and heliospheric activity. Figure 11c shows the PPO periods, where the purple dots show values determined during 1993–2002 from remote Ulysses observations of SKR emissions whose polarization was not determined, such that the hemisphere of the source remains unknown [*Galopeau and Lecacheux*, 2000; *Gurnett et al.*, 2010]. The blue and red data then indicate the northern and southern periods during the Cassini era, respectively, derived from both magnetic field (solid lines) and SKR observations (dotted lines). Specifically, the in-orbit values determined from magnetic field data were derived by *Andrews et al.* [2012] during 2005–2011, *Provan et al.* [2013, 2014] for 2011–2012, and in the present study for 2013–2015, while those derived from SKR data were determined by *Lamy* [2011] during 2004–2010, *Provan et al.* [2014] for 2011–2012, and in the present study for 2013–2015.

It is evident from the data in Figure 11c that the northern and southern PPO periods are strongly seasonally conditioned, possibly through variations in the conductivity of the two polar ionospheres, with the prenorthern solstice northern period approaching similar values to those of the southern solstice southern period observed between ~1999 and ~2008. The latter southern periods reached peaks of ~10.83 h in the postequinox and pre-equinox intervals, though with a shallow minimum value of ~10.77 h occurring close to southern solstice itself. Saturn season is clearly not the only variable concerned, however, since the
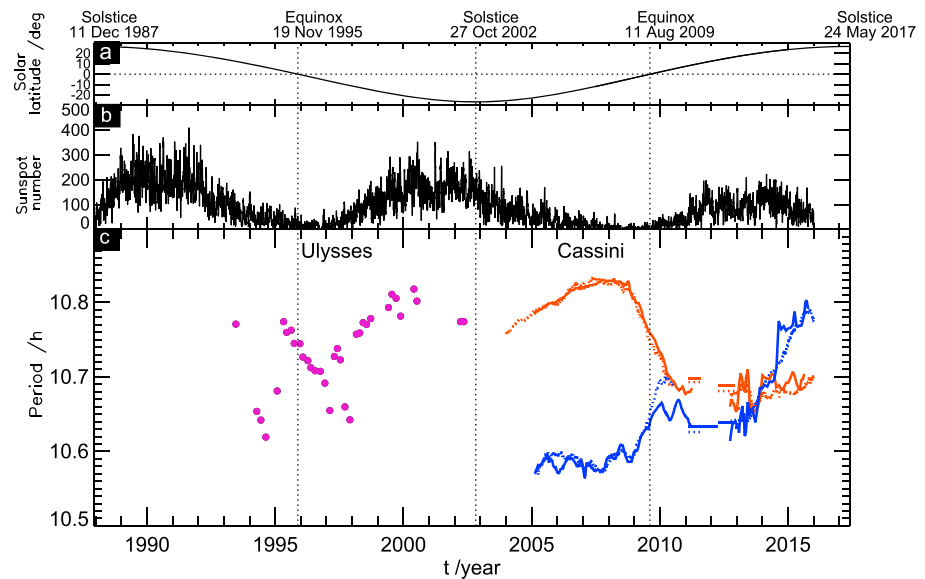
Figure 11. Seasonal conditions, solar conditions, and PPO periods over one Saturn year from northern solstice in December 1987 to northern solstice in May 2017. (a) The planetocentric latitude of the Sun at Saturn, with the times of equinoxes and solstices marked at the top of the plot and by the vertical dotted lines. (b) Daily sunspot numbers. (c) Northern (blue) and southern (red) PPO periods. The filled circles were determined from remote Ulysses SKR observations [*Gurnett et al.*, 2010] and are shown purple since the hemisphere of emission was not determined from polarization measurements. For the Cassini data, solid and dotted lines correspond to values determined from magnetic field and SKR data, respectively. The SKR values were determined by *Lamy* [2011] in 2004–2010, *Provan et al.* [2014] in 2011–2012, and in the present study in 2013–2015. The Cassini magnetic field data were determined by *Andrews et al.* [2012] in 2005–2011, *Provan et al.* [2013, 2014] in 2011–2012, and in the present study in 2013–2015.

behavior of the periods following vernal equinox in mid-2009 and the previous spring equinox in late 1995 were clearly different, irrespective of the hemispheric interpretation of the Ulysses data. While the latter data have reasonably been interpreted by *Gurnett et al.* [2010] as indicating a "clean" reversal in northern and southern PPO periods occurring ~1 year after spring equinox in November 1995, a similar convergence in periods ~1 year after vernal equinox in August 2009 was followed by a ~4 year interval of closely spaced or coalesced periods before an enduring reversal took place ~5 years after equinox and ~3 years before northern solstice, as reported here. In addition, even at that point, the southern period had not simultaneously decreased to similar values to the northern period during southern summer conditions, which reached as low as ~10.58 h. A simple seasonal conductivity effect would also be expected to show near symmetry about the equinox itself due to the essentially instantaneous ionization response of the atmosphere to insolation, rather than an effect with an apparent response delay of ~1 (Earth) year. The physical origin of this behavior thus remains unclear. Even though the closely spaced periods during the recent postequinox interval may have been weakly modulated at ~100–200 day intervals by heliospheric conditions at Saturn according to the evidence presented by *Provan et al.* [2015], it seems unlikely that differences in solar irradiance or heliospheric conditions were responsible. As can be seen in Figure 11b, due to the similarity in the period of the sunspot cycle and the half period of the Saturn year, rather similar solar conditions pertained throughout the two postequinox intervals shown, corresponding initially to solar minimum followed by the ascending phase of the solar cycle. An additional possibility concerns the processes that couple the thermosphere-ionosphere-magnetosphere system to rotation in the middle and lower atmosphere, which must after all set the near-planetary rotation period that governs the PPO phenomenon at zeroth-order level. In this regard we note the singular occurrence of the Great White Spot tropospheric storm whose unexpectedly early onset in December 2010 approximately coincided with the beginning of the interval of closely spaced but unreversed periods and which is known to have resulted in significant temperature and flow perturbations at stratospheric levels for several years thereafter [see, e.g., *Fletcher et al.*, 2012; *Cowley and Provan*, 2013, and references therein]. Although the effects of the storm were principally confined to moderate northern latitudes, it remains conceivable that this affected the generation or upward propagation of waves that transfer

angular momentum through the atmosphere and generate the PPO-related thermospheric flows [e.g., *Fischer et al.*, 2014; *Smith et al.*, 2016, and references therein].

Appendix A: Examples of Magnetic Field Data Employed in the Study

In this appendix we show some typical examples of the magnetic field data from which PPO amplitude and phase values have been obtained as outlined in section 2.1. Specifically, in Figures A1, A2, A3 we present relevant sections of data from three spacecraft Revs with different orbit characteristics, namely, Revs 183, 196, and 221, and show the intervals selected for analysis and the results obtained therefrom, summarized in Table A1.

Figure A1 shows periapsis pass data spanning $t = 3353 - 3358$ days from Rev 183. As seen in Figure 2, this was a highly inclined orbit with a short ~12 day period and a periapsis at ~8 R_S radial distance at ~33° latitude and ~2.8 h LT in the postmidnight sector, such that both polar and core (dipole $L \leq 12$) PPO oscillations were observed. These data also correspond to the initial study interval with small separation of the PPO periods, southern longer than northern, prior to period coalescence (Figure 4). Figures A1a, A1c, and A1e show the residual magnetic field components in spherical polar coordinates referenced to Saturn's northern spin and magnetic pole, r, θ, and ϕ, respectively, after subtraction of the *Burton et al.* [2010] internal planetary field (whose azimuthal component we note is zero). These data were then band-pass filtered between 5 and 20 h using a standard Lanzcos filter to extract the PPO signal, as described in section 2.1, with results shown for the three field components correspondingly in Figures A1b, A1d, and A1f. Figure A1g also shows the radial distance of the spacecraft (solid line), and the dipole L value (dotted line), where the horizontal dashed line at $L = 12$, indicates the maximum extent of the core region. The pairs of vertical red, green, and blue dotted lines then indicate the intervals selected for PPO analysis as quantified in Table A1, corresponding with increasing time to the quiet field of the southern tail lobe (B_r negative), core data obtained in the vicinity of the near-periapsis equatorial crossing, and the quiet field of the northern tail lobe (B_r negative), respectively. The results will be briefly discussed below.

Figures A1h–A1j show the relevant segment of the spacecraft trajectory projected onto the *X-Y*, *X-Z*, and *Y-Z* planes, respectively, where the arrowhead indicates the direction of motion. Here the *Z* axis is aligned with the planet's spin and magnetic axis, the *X-Z* plane contains the Sun, and the *Y* axis completes the right-handed triad pointing toward dusk. The red, green, and blue segments of the trajectory correspond to the intervals selected for analysis indicated by the correspondingly colored vertical dotted lines in Figures A1a–A1g. The dotted and dashed lines show the bow shock and magnetopause locations for a typical solar wind dynamic pressure of 0.03 nPa, according to the models of *Masters et al.* [2008] and *Kanani et al.* [2010], respectively.

As also outlined in section 2.1, data from the selected intervals are least squares fitted to the rotating function given by equation (3), using a guide phase corresponding to a fixed period of 10.70 h given by equations (4a) and (4b), thus yielding values for the PPO amplitude B_{0i} and phase ψ_i relative to the guide phase (modulo 360°) for each field component i. Specifically, the data employed in the fits for Rev 183 are the filtered residual data for all three field components in the two tail lobes and unfiltered B_φ data (only) in the core region. The filtered data are not employed in the core region in this case due to the shortness of the interval concerned, less than a full oscillation, while the core r and θ component data are not included because their variations in the core region are dominated by ring current effects rather than by the PPOs, as can be seen in Figure A1. The best fit models are shown by the red, green, and blue lines overplotted on the data in the intervals between the correspondingly colored vertical dashed lines. Results for the amplitude $B_{0i}B_{0i}$ and phase relative to the guide phase ψ_i are given in Table A1, together with the RMS deviation of the data from the best fit model, given as an indicator of the quality of the fit. Examination of these data first shows that the RMS deviation is smaller than the amplitude in all cases, indicating an acceptable fit, as can also be seen directly by comparison of the data and the best fit model in Figure A1. It can also be seen in Figure A1 and Table A1 that the relative phase values in the two polar regions closely follow expectations outlined in section 2.1. Specifically, to a close approximation, in the south polar region the r and θ components oscillate in phase such that relative phases $\psi_\theta \approx \psi_r$ in Table A1, while the φ component oscillates in leading quadrature with both such that $\psi_\varphi \approx \psi_r - 90° \approx \psi_\theta - 90°$. In the north polar region, however, the r and θ components oscillate in antiphase such that $\psi_\theta \approx \psi_r \pm 180°$, while the φ component oscillates in leading quadrature with r and
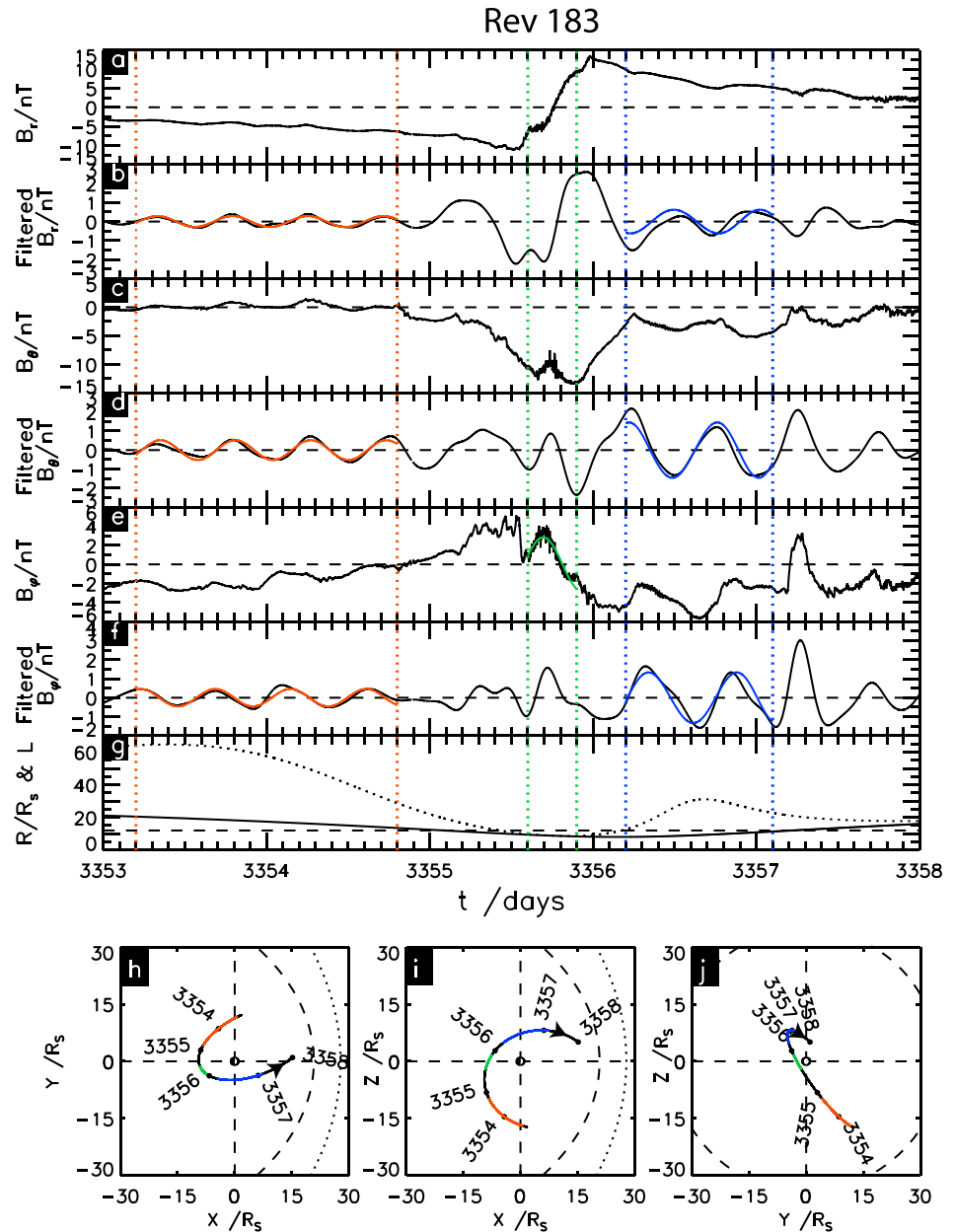
Figure A1. Magnetic field and spacecraft trajectory data for the periapsis pass of Rev 183 spanning $t = 3353 - 3358$ days. (a) The residual r component field data, from which the *Burton et al.* [2010] internal planetary field has been subtracted, while (b) the data after band-pass filtering between 5 and 20 h to extract the PPO signal. (c–f) Corresponding residual and filtered data for the θ and φ field components, though we note that the planetary field model has no azimuthal component so the φ component data are as measured. (g) The radial distance of the spacecraft (solid line) and the dipole L value (dotted line), together with a horizontal dashed line at $L = 12$ indicating the maximum extent of the core field region. The vertical red, green, and blue dotted lines indicate the intervals selected for PPO analysis, corresponding to the southern tail lobe, core region, and northern tail lobe, respectively. Least squares fitting to equation (3) with a guide phase given by equations (4a) and (4b) and a fixed guide period of 10.70 h yields the similarly colored best fit models that are overplotted on the data employed to derive them. Amplitude, relative phase, and RMS deviation data for each fit are given in Table A1. (h–j) The segment of the spacecraft trajectory corresponding to this data interval projected onto the *X-Y*, *X-Z*, and *Y-Z* planes, respectively, where the arrowhead indicates the direction of motion. The *Z* axis is aligned with the Saturn's spin and magnetic axis, the *X-Z* plane contains the Sun, and the *Y* axis completes the right-handed triad pointing toward dusk. The colored segments of the trajectory correspond to the intervals selected for PPO analysis as indicated by the similarly colored vertical dotted lines in Figures A1a–A1g. The dotted and dashed lines in these plots show the bow shock and magnetopause locations for a typical solar wind dynamic pressure of 0.03 nPa [*Masters et al.*, 2008; *Kanani et al.*, 2010].
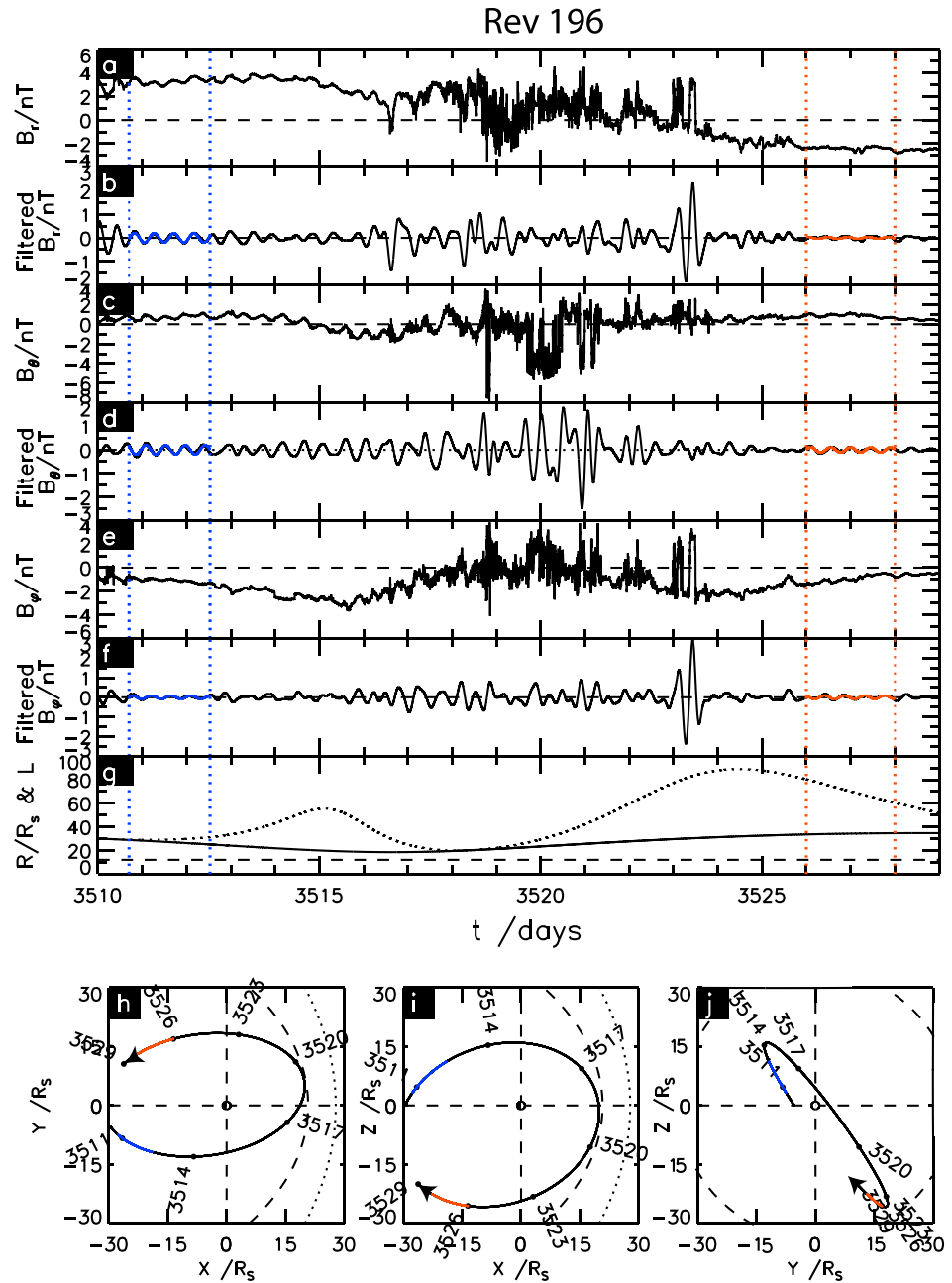
Figure A2. Magnetic field and spacecraft trajectory data for the periapsis pass of Rev 196 spanning $t = 3510 - 3529$ days, in the same format as Figure A1. In this case the data selected for PPO analysis correspond to the northern lobe inbound between the pair of vertical blue lines and the southern lobe outbound between the pair of vertical red lines. The spacecraft did not enter the core region (dipole $L \leq 12$) on this Rev. Fit data are given in Table A1.

lagging quadrature with θ such that $\psi_\varphi \approx \psi_r - 90° \approx \psi_\theta + 90°$. As discussed in section 2.3, when the northern polar phase data are plotted in N-format in Figure 3a and the southern polar phase data in S-format in Figure 3c, they thus form tightly grouped sets of values in both cases. The core region ϕ component fit data result from the vector superposition of the two PPO oscillations with closely equal amplitudes within the core region, as discussed in section 2.5.1 and shown in Figure 5.

Figure A2 similarly shows periapsis pass data spanning $t = 3510 - 3529$ days from Rev 196. As shown in Figure 2, this is also a highly inclined orbit but now with a longer ~22 day period and a periapsis at ~18 R_S
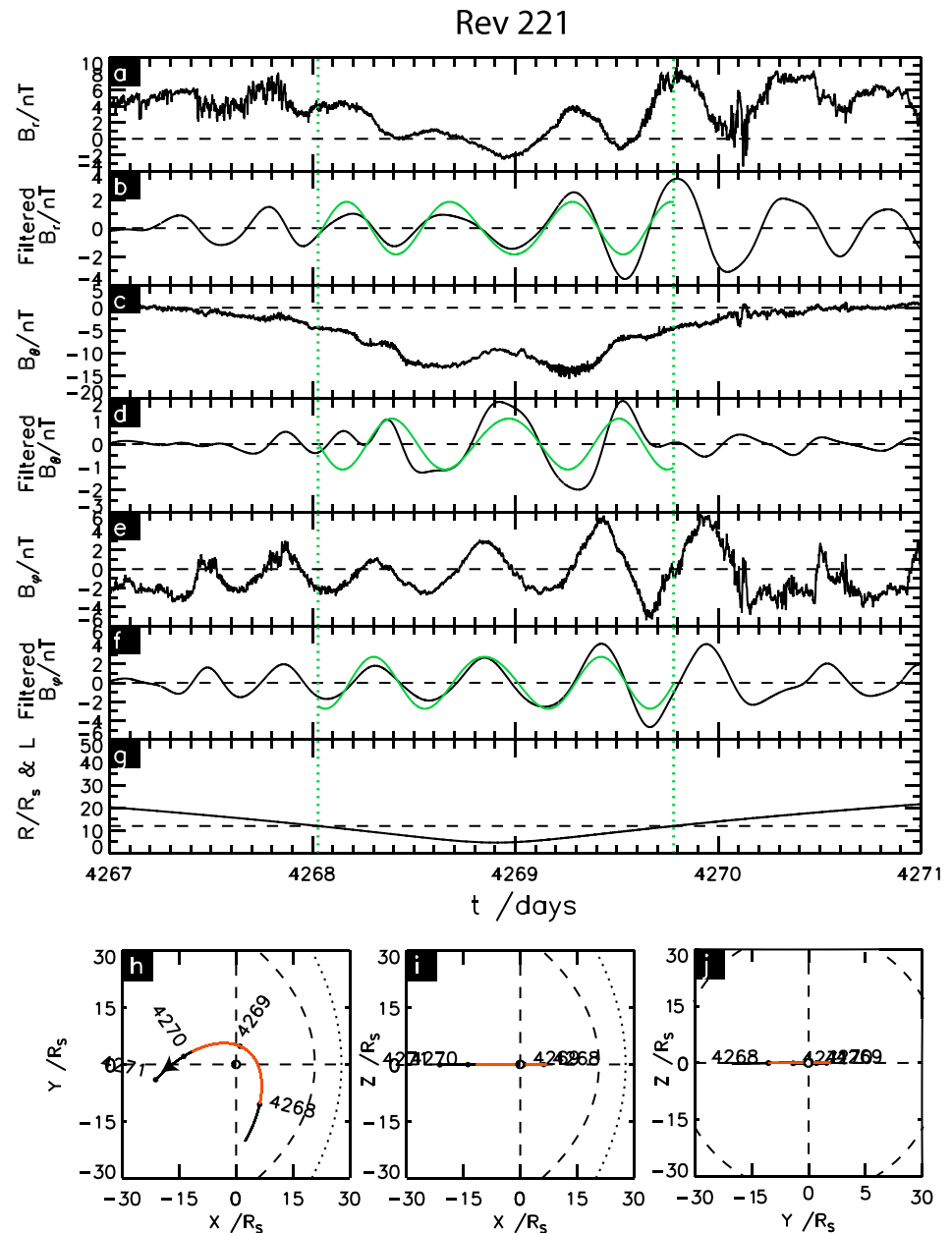
Rev 221

Figure A3. Magnetic field and spacecraft trajectory data for the periapsis pass of Rev 221 spanning $t = 4267 - 4271$ days, in the same format as Figure A1. The data selected for PPO analysis are those of the near-equatorial core region with dipole $L \leq 12$ between the pair of vertical green lines (see Figure A3g). The fit data are given in Table A1.

radial distance at ~38° latitude and ~10.4 h LT in the prenoon sector. In this case PPO oscillations were observed in the quiet fields of the tail lobes both inbound in northern lobe and outbound in the southern lobe as shown by the selected intervals between the blue and red pairs of vertical dotted lines in Figures A2a–A2g, respectively, but due to the larger periapsis distance the dipole L value of the spacecraft reached a minimum value of only $L \approx 20$ as shown in Figure A2g, such that no core data were obtained. We note that these data also correspond to the interval in which the two PPO periods had newly coalesced with a common period of ~10.66 h (at $t \sim 3450$ days), as seen in Figure 4. Perusal of the fit data in Table A1 shows that on the inbound pass in the northern lobe the RMS deviations are again significantly smaller than the PPO amplitudes, indicating three acceptable fits as also can be seen directly in Figure A2. On the outbound pass in the southern lobe, however, the r component amplitude is very small ~0.04 nT and smaller

Table A1. Fit Analysis Results for the Selected Intervals of Revs 183, 196, and 221 Shown in Figures A1, A2, and A3

Rev and Region	183 Southern Polar	183 Core	183 Northern Polar	196 Northern Polar	196 Southern Polar	221 Core
Start time/days	3353.2	3355.6	3356.2	3510.7	3526.0	4268.0
End time/days	3354.8	3355.9	3357.1	3512.5	3528.0	4269.8
B_r fit RMS/nT	0.07	-	0.44	0.05	0.05	0.71
B_r amplitude/nT	0.29	-	0.62	0.20	0.04	1.85
B_r phase/degree	92	-	343	291	46	192
B_θ fit RMS/nT	0.13	-	0.36	0.07	0.03	0.76
B_θ amplitude/nT	0.52	-	1.45	0.20	0.11	1.12
B_θ phase/degree	106	-	157	137	96	357
B_φ fit RMS/nT	0.12	0.58	0.36	0.03	0.04	0.82
B_φ amplitude/nT	0.46	2.84	1.33	0.09	0.09	2.74
B_φ phase/degree	10	126	240	238	347	292

than the RMS deviation of ~0.05 nT, thus indicating an unacceptably poor fit, such that the corresponding phase datum was discarded from further analysis. The opposite is the case for the southern lobe θ and φ component fits with amplitudes significantly larger than the RMS deviations (Table A1), thus indicating acceptable fits. The acceptable fits inbound and outbound are also seen to provide phase values approximately consistent with expectations for the northern and southern lobes as described above, such that they again form tightly grouped phase data sets in Figures 3a and 3c.

Figure A3 shows periapsis pass data spanning $t = 4267 - 4271$ days from Rev 221 toward the end of the study interval, when the spacecraft orbit had returned close to the equatorial plane with a period of ~22 days and a periapsis at ~5 R_S and ~15.5 h LT in the midafternoon sector (see Figure 2). In this case PPO oscillations were observed over an extended ~2 day interval within the equatorial core region, contained between the pair of green vertical dotted lines in Figures A3a–A3g, respectively. These data also correspond to the interval dominated by the northern PPO oscillations after the reversal in periods (which took place at $t \sim 3850$ days), shortly after the southern PPO modulations could no longer be discerned in the core region magnetic field phase data. Perusal of the fit data in Table A1 shows that the RMS deviations are again significantly smaller than the PPO amplitudes for all three field components, thus indicating acceptable fits as can be seen directly in Figure A3. The relative phases are consistent with an essentially pure northern PPO oscillation, with the θ component in antiphase with r, while the φ component is in lagging quadrature with r and thus in leading quadrature with θ. These data thus form a tightly grouped set when plotted in N-format in Figure 3a, while the θ component phase is separated by ~180° from the r and φ component phases when plotted in S-format in Figure 3c, corresponding to almost perfectly ungrouped data.

Appendix B: Aliased Modulation Periods in Magnetic Fit Variance Plots

In the gray scaled plots in Figures 3b and 3d showing the fit variance V versus magnetic oscillation period and time, it is evident that there sometimes exists multiple relatively long-lived local variance minima, additional to the temporally near-continuous minima taken to correspond to the true modulation periods. Here we show that the most prominent of these features are due to aliasing related to the inescapable modulo 360° ambiguity in the absolute phase differences between successive sets of oscillation phase measurements obtained on a Rev-by-Rev basis.

Suppose we measure magnetic oscillation phase Φ at time t, and phase $\Phi + \Delta\Phi$ at time $t + T$, where $\Delta\Phi$ is the true phase difference, and T is the time between phase measurements, essentially the orbital period of the spacecraft. The true oscillation period (equation (2)) is then

$$\tau = \frac{360}{(d\Phi/dt)} = \frac{360 \; T}{\Delta\Phi}, \tag{B1}$$

where as usual the phases are expressed in degrees. As far as the individual phase data are concerned, however, the change in phase between the two measurements could equally be $\Delta\Phi \pm 360N$ deg for any integer $N = 1, \; 2, \; 3 \ldots$, with corresponding aliased periods

$$\tau' = \frac{360 \; T}{\Delta\Phi \pm 360N} = \frac{\tau}{\left(1 \pm \frac{N\tau}{T}\right)}. \tag{B2}$$
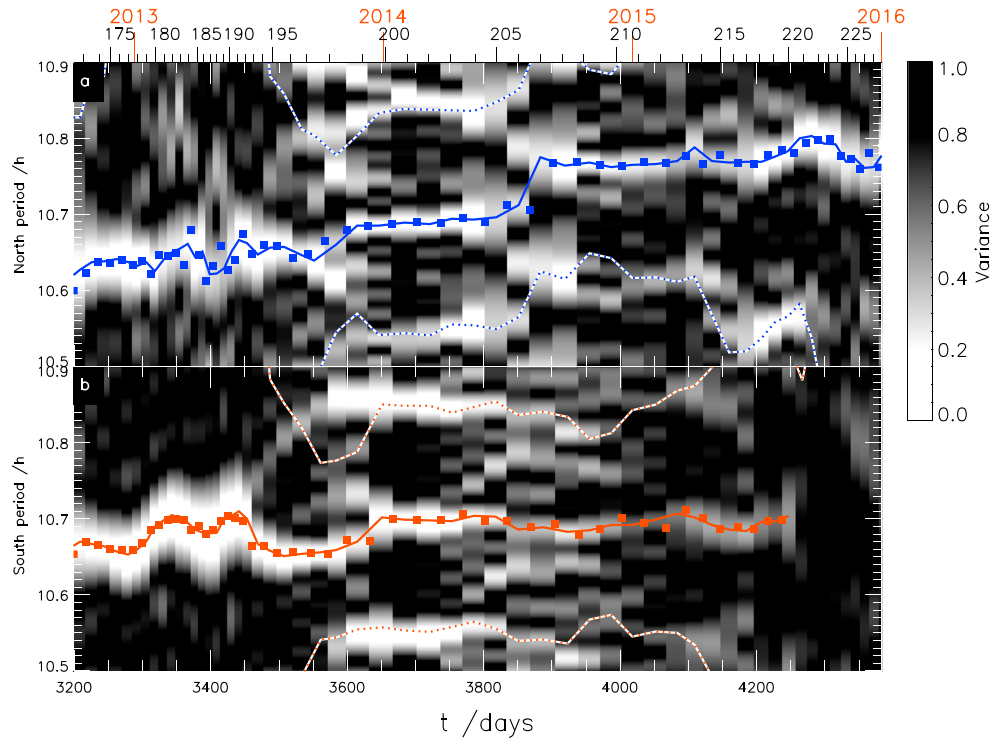
Figure B1. Comparison of aliased period estimates with subsidiary minima in the 5 Rev (or occasionally 3 Rev) fit variances shown in Figures 3b and 3d. (a) The fit variance to the N-format phase data, gray scaled as shown on the right, plotted versus oscillation period and time, with the near-continuous principal minimum taken to correspond to the northern PPO period shown by the blue line and squares, as in Figure 3b. The two $N = 1$ aliased periods given by equation (B3) on either side of the true period are shown by the blue and white dashed lines (using the unapproximated equation). (b) The fit variance to the S-format phase data, with the near-continuous principal minimum taken to correspond to the southern PPO period shown by the red line and squares, as in Figure 3d. The two $N = 1$ aliased periods given by equation (B3) on either side of the true period are shown by the red and white dashed lines.

Here only $N = 1$ is relevant, leading to the pair of aliased periods closest to the true period on either side being given by

$$\tau'_{\pm} = \frac{\tau}{\left(1 \pm \frac{\tau}{T}\right)} \approx \tau \mp \left(\frac{\tau^2}{T}\right), \tag{B3}$$

where the approximate form is valid when the orbital period T is much longer than the oscillation period τ. This effect can thus produce long-lived continuous minima in variance on either side of the minimum associated with the true period during intervals when the orbital period T changes slowly with time. These aliased periods lie far from the true period when the orbital period T is short and approach the true period as T becomes large.

In Figures B1a and B1b we reproduce the data in Figures 3b and 3d showing the fit variances versus modulation period and time for the N- and S-format phase data, respectively, together with the true periods associated with the minimum that is near-continuous across each plot (blue and red lines and squares as in Figure 3). The blue and white dashed lines in Figure B1a and the red and white dashed lines in Figure B1b then show the two $N = 1$ aliased periods in each case given by equation (B3), using the unapproximated form, insofar as they lie inside the plotted range of oscillation periods between 10.5 and 10.9 h. Initially, the orbit period is relatively short, ~11 days (Figure 2e), such that the aliased periods are offset from the true period by ~ ±0.4 h (equation (B3)) and thus well off-scale in these figures. After $t \approx 3600$ days, however, the orbital period lengthens to ~35 days, resulting in the two aliased periods appearing on either side of the true period in both Figures B1a and B1b with offsets ~ ±0.15 h. These subsidiary minima can be followed in the data for much of the following interval while they remain on-scale, notably receding from the true period in Figure B1a around ~4150 days as the orbital period reduces to ~15–20 days, corresponding to offsets of ~ ±0.25 h. Overall, the aliased periods given by equation (B3) are seen to give a good account of the longer-lived subsidiary variance minima in Figures 3b and 3d.

References

Andrews, D. J., E. J. Bunce, S. W. H. Cowley, M. K. Dougherty, G. Provan, and D. J. Southwood (2008), Planetary period oscillations in Saturn's magnetosphere: Phase relation of equatorial magnetic field oscillations and SKR modulation, *J. Geophys. Res.*, 113, A09205, doi:10.1029/2007JA012937.

Andrews, D. J., S. W. H. Cowley, M. K. Dougherty, and G. Provan (2010a), Magnetic field oscillations near the planetary period in Saturn's equatorial magnetosphere: Variation of amplitude and phase with radial distance and local time, *J. Geophys. Res.*, 115, A04212, doi:10.1029/2007JA014729.

Andrews, D. J., A. J. Coates, S. W. H. Cowley, M. K. Dougherty, L. Lamy, G. Provan, and P. Zarka (2010b), Magnetospheric period oscillations at Saturn: Comparison of equatorial and high-latitude magnetic field periods with north and south SKR periods, *J. Geophys. Res.*, 115, A12252, doi:10.1029/2010JA015666.

Andrews, D. J., B. Cecconi, S. W. H. Cowley, M. K. Dougherty, L. Lamy, G. Provan, and P. Zarka (2011), Planetary period oscillations in Saturn's magnetosphere: Evidence in magnetic field phase data for rotational modulation of Saturn kilometric radiation emissions, *J. Geophys. Res.*, 116, A09206, doi:10.1029/2011JA016636.

Andrews, D. J., S. W. H. Cowley, M. K. Dougherty, L. Lamy, G. Provan, and D. J. Southwood (2012), Planetary period oscillations in Saturn's magnetosphere: Evolution of magnetic oscillation properties from southern summer to post-equinox, *J. Geophys. Res.*, 117, A04224, doi:10.1029/2011JA017444.

Arridge, C. S., et al. (2011), Periodic motion of Saturn's nightside plasma sheet, *J. Geophys. Res.*, 116, A11205, doi:10.1029/2011JA016827.

Burch, J. L., A. D. DeJong, J. Goldstein, and D. T. Young (2009), Periodicity in Saturn's magnetosphere: Plasma cam, *Geophys. Res. Lett.*, 36, L14203, doi:10.1029/2009GL039043.

Burton, M. E., M. K. Dougherty, and C. T. Russell (2010), Saturn's internal planetary magnetic field, *Geophys. Res. Lett.*, 37, L24105, doi:10.1029/2010GL045148.

Carbary, J. F., and S. M. Krimigis (1982), Charged particle periodicity in the Saturnian magnetosphere, *Geophys. Res. Lett.*, 9, 1073–1076, doi:10.1029/GL009i009p01073.

Cecconi, B., L. Lamy, P. Zarka, R. Prangé, W. S. Kurth, and P. Louarn (2009), Gonipolarimetric study of the revolution 29 perikrone using the Cassini Radio and Plasma Wave Science instrument high-frequency radio receiver. *J. Geophys. Res.*, 114, A03215, doi:10.1029/2008JA013830.

Cowley, S. W. H., and G. Provan (2013), Saturn's magnetospheric planetary period oscillations, neutral atmosphere circulation, and thunderstorm activity: Implications, or otherwise, for physical links, *J. Geophys. Res. Space Physics*, 118, 7246–7261, doi:10.1002/2013JA019200.

Cowley, S. W. H., and G. Provan (2015), Planetary period oscillations in Saturn's magnetosphere: Comments on the relation between post-equinox periods determined from magnetic field and SKR emission data, *Ann. Geophys.*, 33, 901–912, doi:10.5194/angeo-33-901-2015.

Cowley, S. W. H., and G. Provan (2016), Planetary period oscillations in Saturn's magnetosphere: Further comments on the relationship between post-equinox properties deduced from magnetic field and Saturn kilometric radiation measurements, *Icarus*, 272, 258–276, doi:10.1016/j.icarus.2016.02.051.

Cowley, S. W. H., D. M. Wright, E. J. Bunce, A. C. Carter, M. K. Dougherty, G. Giampieri, J. D. Nichols, and T. R. Robinson (2006), Cassini observations of planetary-period magnetic field oscillations in Saturn's magnetosphere: Doppler shifts and phase motion, *Geophys. Res. Lett.*, 33, L07104, doi:10.1029/2005GL025522.

Cowley, S. W. H., G. Provan, and D. J. Andrews (2015), Comment on "Magnetic phase structure of Saturn's 10.7 hour oscillations" by Yates et al, *J. Geophys. Res. Space Physics*, 120, 5686–5690, doi:10.1002/2015JA021351.

Cowley, S. W. H., P. Zarka, G. Provan, L. Lamy, and D. J. Andrews (2016), Comment on "A new approach to Saturn's periodicities" by J. F. Carbary, *J. Geophys. Res. Space Physics*, 121, 2418–2422, doi:10.1002/2015JA021996.

Desch, M. D., and M. L. Kaiser (1981), Voyager measurement of the rotation period of Saturn's magnetic field, *Geophys. Res. Lett.*, 8, 253–256, doi:10.1029/GL008i003p00253.

Espinosa, S. A., and M. K. Dougherty (2000), Periodic perturbations in Saturn's magnetic field, *Geophys. Res. Lett.*, 27, 2785–2788, doi:10.1029/2000GL000048.

Fischer, G., B. Cecconi, L. Lamy, S.-Y. Ye, U. Taubenschuss, W. Macher, P. Zarka, W. S. Kurth, and D. A. Gurnett (2009), Elliptical polarization of Saturn kilometric radiation observed from high latitudes, *J. Geophys. Res.*, 114, A08216, doi:10.1029/2009JA014176.

Fischer, G., S.-Y. Ye, J. B. Groene, A. P. Ingersoll, K. M. Sayanagi, J. D. Menietti, W. S. Kurth, and D. A. Gurnett (2014), A possible influence of the Great White Spot on Saturn kilometric radiation periodicity, *Ann. Geophys.*, 32, 1463–1476, doi:10.5194/angeo-32-1463-2014.

Fischer, G., D. A. Gurnett, W. S. Kurth, S.-Y. Ye, and J. B. Groene (2015), Saturn kilometric radiation periodicity after equinox, *Icarus*, 254, 72–91, doi:10.1016/j.icarus.2015.03.014.

Fletcher, L. N., et al. (2012), The origin and evolution of Saturn's 2011-2012 stratospheric vortex, *Icarus*, 221, 560–586, doi:10.1016/j.icarus.2012.08.024.

Galopeau, P. H. M., and A. Lecacheux (2000), Variations of Saturn's radio rotation period measured at kilometer wavelengths, *J. Geophys. Res.*, 105, 13,089–13,101, doi:10.1029/1999JA005089.

Gurnett, D. A., A. Lecacheux, W. S. Kurth, A. M. Persoon, J. B. Groene, L. Lamy, P. Zarka, and J. F. Carbary (2009a), Discovery of a north-south asymmetry in Saturn's radio rotation period, *Geophys. Res. Lett.*, 36, L16102, doi:10.1029/2009GL039621.

Gurnett, D. A., A. M. Persoon, J. B. Groene, A. J. Kopf, G. B. Hospodarsky, and W. S. Kurth (2009b), A north-south difference in the rotation rate of auroral hiss at Saturn: Comparison to Saturn's kilometric radio emission, *Geophys. Res. Lett.*, 36, L21108, doi:10.1029/2009GL040774.

Gurnett, D. A., J. B. Groene, A. M. Persoon, J. D. Menietti, S.-Y. Ye, W. S. Kurth, R. J. MacDowell, and A. Lecacheux (2010), The reversal of the rotational modulation rates of the north and south components of Saturn kilometric radiation near equinox, *Geophys. Res. Lett.*, 37, L24101, doi:10.1029/2010GL045796.

Gurnett, D. A., J. B. Groene, T. F. Averkamp, W. S. Kurth, S.-Y. Ye, and G. Fischer (2011), The SLS4 longitude system based on a tracking filter analysis of the rotational modulation of Saturn kilometric radiation, in *Planetary Radio Emissions VII*, edited by H. O. Rucker et al., pp. 51–64 , Austrian Acad. Sci. Press, Vienna.

Hunt, G. J., S. W. H. Cowley, G. Provan, E. J. Bunce, I. I. Alexeev, E. S. Belenkaya, V. V. Kalegaev, M. K. Dougherty, and A. J. Coates (2014), Field-aligned currents in Saturn's southern nightside magnetosphere: Subcorotation and planetary period oscillation components, *J. Geophys. Res. Space Physics*, 119, 9847–9899, doi:10.1002/2014JA020506.

Hunt, G. J., S. W. H. Cowley, G. Provan, E. J. Bunce, I. I. Alexeev, E. S. Belenkaya, V. V. Kalegaev, M. K. Dougherty, and A. J. Coates (2015), Field-aligned currents in Saturn's northern nightside magnetosphere: Evidence for inter-hemispheric current flow associated with planetary period oscillations, *J. Geophys. Res. Space Physics*, 120, 7552–7584, doi:10.1002/2015JA021454.

Jia, X., and M. G. Kivelson (2012), Driving Saturn's magnetospheric periodicities from the upper atmosphere/ionosphere: Magnetotail response to dual sources, *J. Geophys. Res.*, 117, A11219, doi:10.1029/2012JA018183.

Jia, X., M. G. Kivelson, and T. I. Gombosi (2012), Driving Saturn's magnetospheric periodicities from the upper atmosphere/ionosphere, *J. Geophys. Res.*, *117*, A04215, doi:10.1029/2011JA017367.

Jinks, S. L., et al. (2014), Cassini multi-instrument assessment of Saturn's polar cap boundary, *J. Geophys. Res. Space Physics*, *119*, 8161–8177, doi:10.1002/2014JA020367.

Kaiser, M. L., M. D. Desch, W. S. Kurth, A. Lecacheux, F. Genova, B. M. Pedersen, and D. R. Evans (1984), Saturn as a radio source, in *Saturn*, edited by T. Gehrels and M. S. Matthews, pp. 378–415, Univ. Ariz. Press, Tucson.

Kanani, S. J., et al. (2010), A new form of Saturn's magnetopause using a dynamic pressure balance model, based on in situ, multi-instrument Cassini measurements, *J. Geophys. Res.*, *115*, A06207, doi:10.1029/2009JA014262.

Kimura, T., et al. (2013), Long-term modulations of Saturn's auroral radio emissions by the solar wind and seasonal variations controlled by the solat ultraviolet flux, *J. Geophys. Res. Space Physics*, *118*, 7019–7035, doi:10.1002/2013JA018833.

Kurth, W. S., T. F. Averkamp, D. A. Gurnett, J. B. Groene, and A. Lecacheux (2008), An update to a Saturnian longitude system based on kilometric radio emissions, *J. Geophys. Res.*, *113*, A05222, doi:10.1029/2007JA012861.

Lamy, L. (2011), Variability of southern and northern SKR periodicities, in *Planetary Radio Emissions VII*, edited by H. O. Rucker et al., pp. 39–50, Austrian Acad. Sci. Press, Vienna.

Lamy, L., P. Zarka, B. Cecconi, R. Prangé, W. S. Kurth, and D. A. Gurnett (2008a), Saturn kilometric radiation: Average and statistical properties, *J. Geophys. Res.*, *113*, A07201, doi:10.1029/2007JA012900.

Lamy, L., P. Zarka, B. Cecconi, S. Hesse, and R. Prangé (2008b), Modeling of Saturn kilometric radiation arcs and equatorial shadow zone, *J. Geophys. Res.*, *113*, A10213, doi:10.1029/2008JA013464.

Lamy, L., B. Cecconi, R. Prangé, P. Zarka, J. D. Nichols, and J. T. Clarke (2009), An auroral oval at the footprint of Saturn's kilometric radio sources, co-located with the UV aurorae, *J. Geophys. Res.*, *114*, A10212, doi:10.1029/2009JA014401.

Lamy, L., et al. (2010), Properties of Saturn kilometric radiation measured within its source region, *Geophys. Res. Lett.*, *37*, L12104, doi:10.1029/2010GL043415.

Lamy, L., B. Cecconi, P. Zarka, P. Canu, P. Schippers, W. S. Kurth, R. L. Mutel, D. A. Gurnett, D. Menietti, and P. Louarn (2011), Emission and propagation of Saturn kilometric radiation: Magnetoionic modes, beaming pattern, and polarization state, *J. Geophys. Res.*, *116*, A04212, doi:10.1029/2010JA016195.

Lamy, L., R. Prangé, W. Pryor, J. Gustin, S. V. Badman, H. Melin, T. Stallard, D. G. Mitchell, and P. C. Brandt (2013), Multispectral diagnosis of Saturn's aurorae throughout a planetary rotation, *J. Geophys. Res. Space Physics*, *118*, 4817–4843, doi:10.1002/jgra.50404.

Mardia, K. V., and P. E. Jupp (2000), *Directional Statistics*, John Wiley, Chichester, U. K.

Masters, A., N. Achilleos, M. K. Dougherty, J. A. Slavin, G. B. Hospodarsky, C. S. Arridge, and A. J. Coates (2008), An empirical model of Saturn's bow shock: Cassini observations of shock location and shape, *J. Geophys. Res.*, *113*, A10210, doi:10.1029/2008JA013276.

Menietti, J. D., R. L. Mutel, P. Schippers, S.-Y. Ye, D. A. Gurnett, and L. Lamy (2011), Analysis of Saturn kilometric radiation near a source center, *J. Geophys. Res.*, *116*, A12222, doi:10.1029/2011JA017056.

Mutel, R. L., J. D. Menietti, D. A. Gurnett, W. Kurth, P. Schippers, C. Lynch, L. Lamy, C. Arridge, and B. Cecconi (2010), CMI growth rates for Saturnian kilometric radiation, *Geophys. Res. Lett.*, *37*, L19105, doi:10.1029/2010GL044940.

Provan, G., D. J. Andrews, C. S. Arridge, S. W. H. Cowley, S. E. Milan, M. K. Dougherty, and D. M. Wright (2009), Polarization and phase of planetary period oscillations on high latitude field lines in Saturn's magnetosphere, *J. Geophys. Res.*, *114*, A02225, doi:10.1029/2008JA013782.

Provan, G., D. J. Andrews, B. Cecconi, S. W. H. Cowley, M. K. Dougherty, L. Lamy and P. Zarka (2011), Magnetospheric period magnetic field oscillations at Saturn: Equatorial phase "jitter" produced by superposition of southern- and northern-period oscillations, *J. Geophys. Res.*, *116*, A04225, doi:10.1029/2010JA016213.

Provan, G., D. J. Andrews, C. S. Arridge, A. J. Coates, S. W. H. Cowley, G. Cox, M. K. Dougherty, and C. M. Jackman (2012), Dual periodicities in planetary-period magnetic field oscillations in Saturn's tail, *J. Geophys. Res.*, *117*, A01209, doi:10.1029/2011JA017104.

Provan, G., S. W. H. Cowley, J. Sandhu, D. J. Andrews, and M. K. Dougherty (2013), Planetary period magnetic field oscillations in Saturn's magnetosphere: Post-equinox abrupt non-monotonic transitions to northern system dominance, *J. Geophys. Res. Space Physics*, *118*, 3243–3264, doi:10.1002/jgra.50186.

Provan, G., L. Lamy, S. W. H. Cowley, and M. K. Dougherty (2014), Planetary period oscillations in Saturn's magnetosphere: Comparison of magnetic oscillations and SKR modulations in the post-equinox interval, *J. Geophys. Res. Space Physics*, *119*, 7380–7401, doi:10.1002/2014JA020011.

Provan, G., C. Tao, S. W. H. Cowley, M. K. Dougherty, and A. J. Coates (2015), Planetary period oscillations in Saturn's magnetosphere: Examining a possible relationship between abrupt changes in the behavior of the planetary period oscillations and solar wind-induced magnetospheric compressions and expansions, *J. Geophys. Res. Space Physics*, *120*, 9524–9544, doi:10.1002/2015JA021642.

Sandel, B. R., and A. L. Broadfoot (1981), Morphology of Saturn's aurora, *Nature*, *292*, 679–682, doi:10.1038/292679a0.

Sandel, B. R., et al. (1982), Extreme ultraviolet observations from the Voyager 2 encounter with Saturn, *Science*, *215*, 548–553, doi:10.1126/science.215.4532.548.

Smith, C. G. A., L. C. Ray, and N. A. Achilleos (2016), A planetary wave model for Saturn's 10.7-h periodicities, *Icarus*, *268*, 76–88, doi:10.1016/j.icarus.2015.12.041.

Southwood, D. J. (2011), Direct evidence of differences in magnetic rotation rate between Saturn's northern and southern polar regions, *J. Geophys. Res.*, *116*, A01201, doi:10.1029/2010JA016070.

Southwood, D. J., and S. W. H. Cowley (2014), The origin of Saturn magnetic periodicities: Northern and southern current systems, *J. Geophys. Res. Space Physics*, *119*, 1563–1571, doi:10.1029/2013JA019632.

Southwood, D. J., and M. G. Kivelson (2007), Saturn magnetospheric dynamics: Elucidation of a camshaft model, *J. Geophys. Res.*, *112*, A12222, doi:10.1029/2007JA012254.

Warwick, J. W., et al. (1981), Planetary radio astronomy observations from Voyager-1 near Saturn, *Science*, *212*, 239–243, doi:10.1126/science.212.4491.239.

Warwick, J. W., D. S. Evans, J. H. Romig, J. K. Alexander, M. D. Desch, M. L. Kaiser, M. Aubier, Y. Leblanc, A. Lecacheux, and B. M. Pedersen (1982), Planetary radio astronomy observations from Voyager-2 near Saturn, *Science*, *215*, 582–587, doi:10.1126/science.215.4532.582.